Planetary and Space Science 209 (2021) 105373

Contents lists available at ScienceDirect

Planetary and Space Science

journal homepage: www.elsevier.com/locate/pss

CaSSIS color and multi-angular observations of Martian slope streaks

A. Valantinas [a,*], P. Becerra [a], A. Pommerol [a], L.L. Tornabene [b], L. Affolter [a], G. Cremonese [c], E. Hauber [d], A.S. McEwen [e], G. Munaretto [c], M. Pajola [c], A. Parkes Bowen [f], M.R. Patel [g], V.G. Rangarajan [b], N. Schorghofer [h], N. Thomas [a]

[a] Physikalisches Institut, Universität Bern, Sidlerstrasse 5, 3012, Bern, Switzerland
[b] Institute for Earth & Space Exploration, Dept. of Earth Sciences, Western University, London, Canada
[c] Osservatorio Astronomico di Padova, INAF, Padova, Italy
[d] Deutsches Zentrum für Luft-und Raumfahrt, Institut für Planetenforschung, Berlin, Germany
[e] Lunar and Planetary Lab, University of Arizona, Tucson, USA
[f] Space Research Centre, School of Physics and Astronomy, University of Leicester, Leicester, UK
[g] Open University, Milton-Keynes, UK
[h] Planetary Science Institute, Tucson, USA

ARTICLE INFO

Keywords:
Slope streaks
Mars
CaSSIS
Reflectance spectroscopy
Regolith

ABSTRACT

Slope streaks are albedo features that form frequently on equatorial Martian slopes. Most slope streaks are dark relative to surrounding terrains, a minor fraction is bright, and there are rare transitioning streaks that exhibit a contrast reversal partway downslope. Their formation mechanisms and physical surface properties are not well understood. New observations acquired by the Colour and Stereo Surface Imaging System (CaSSIS) on board ESA's ExoMars Trace Gas Orbiter (TGO) provide insights into slope streaks' surface microstructure, roughness and particle size ranges. Using multiple phase angle observations, we show that dark slope streaks are substantially rougher and possibly more porous than their bright counterparts, which are likely composed of more compact regolith. Color data acquired in the four wavelength bands suggest that dark streaks are spectrally similar to bright streaks but are composed of larger particles. The comparison of our orbital results to the laboratory measurements of Martian regolith analogs indicates that particles within dark slope streaks may be up to a factor of four larger than the granular material of the surrounding terrains. At one study site in Arabia Terra, using complementary imagery from other orbiters, we identify a case where dark slope streaks turned fully bright in a twenty-year period. These and CaSSIS observations suggest that bright slope streaks are old dark slope streaks, likely formed by deposition of dust or decomposition of surface aggregates into smaller particles.

1. Introduction

The surface of contemporary Mars hosts a variety of active geologic processes (Dundas et al., 2021). Linear and fan-shaped albedo features, known as dark slope streaks, were discovered in Viking orbiter images of the Olympus Mons aureole (Morris, 1982). Knowledge about their global extent and formation mechanism was considerably expanded using the Mars Global Surveyor (MGS) Mars Orbiter Camera (MOC; Malin and Edgett, 2001) datasets (Sullivan et al., 2001; Schorghofer et al., 2007). Very high image resolution (~0.3 m/px) analysis studies based on the Mars Reconnaissance Orbiter (MRO) High Resolution Imaging Experiment (HiRISE; McEwen et al., 2007) revealed further information about slope streak morphology and aeolian surface evolution (e.g. Chuang et al., 2010). Slope streaks are found in equatorial, high albedo and low thermal inertia regions that are covered by a fine surface particle layer (Ruff and Christensen, 2002). Within the forty years of orbital observations of slope streaks several hypotheses have been raised to explain their origin. Initially proposed to be debris weathered from dark pyroclastic materials (Morris, 1982), a dry model where avalanching surface dust exposes a deeper, darker, and presumably less oxidized Martian substrate was subsequently suggested (Williams, 1991; Sullivan et al., 2001; Dundas, 2020b). The latter model was supported by low-sun illumination HiRISE observations, which showed that a surface layer is removed, at least in large slope streaks (Phillips et al., 2007; Chuang et al., 2007). Conversely, several properties of slope streaks have been proposed as evidence for fluid-related formation mechanisms. Slope streak ability to

* Corresponding author.
E-mail address: adomas.valantinas@unibe.ch (A. Valantinas).

https://doi.org/10.1016/j.pss.2021.105373
Received 10 June 2021; Received in revised form 22 October 2021; Accepted 28 October 2021
Available online 1 November 2021

initiate well below the angle of repose (Brusnikin et al., 2016) and exhibit bifurcating morphology (Miyamoto et al., 2004), the presence of a fine particle layer that slows desiccation (Ferguson and Lucchitta, 1984) and allows capillarity (Kreslavsky and Head, 2009); and the regional detection of chloride-rich chemistry (Bhardwaj et al., 2017) have all been inferred to support fluid formation models.

Slope streaks are known to be darker than their surrounding material by ~10% (Sullivan et al., 2001). The various contrast states of slope streak darkness suggested that a time-dependent fading mechanism likely related to dust deposition is occurring (Aharonson et al., 2003). Some streaks have been observed to fade on timescales of four decades (Bergonio et al., 2013) and generally persist longer than the seasonal occurrences of dust devil tracks (Balme et al., 2003). While slope streaks have been observed to form sporadically (Schorghofer and King, 2011), seasonal formation has also been recently indicated (Heyer et al., 2019).

On Mars, a peculiar type of slope streaks that are brighter than their surroundings by up to 2% are known to exist (Sullivan et al., 2001). Bright streaks might appear on the same slope as dark streaks, and remain visible under varying lighting geometry conditions (Schorghofer et al., 2007). Initially it was proposed that bright streaks form in a thinner particle layer (Sullivan et al., 2001). However, the absence of newly formed bright slope streaks suggested that bright slope steaks are simply old dark slope streaks (Schorghofer et al., 2007). A rare transitioning case in which slope streak brightness contrast reverses partway downslope was observed and suggested to be either an angular unconformity (Sullivan et al., 2001) or viewing angle effect (Baratoux et al., 2006).

Using hyperspectral images from the Compact Reconnaissance Imaging Spectrometer for Mars (CRISM; Murchie et al., 2007) and HiRISE color photometry, Mushkin et al. (2010) found that slope streaks are spectrally featureless at the visible and near-infrared wavelengths. They concluded that dark slope streaks appear dark not due to an exposure of the pre-existing substrate, as suggested by the avalanching dust model (Sullivan et al., 2001), but due to soil enrichment of low-albedo ferric oxides and amalgamation of nanophase FeOx grains into larger particles. They argued that slope streak surfaces are dry, but a short-lived liquid phase was needed to explain the particle agglomeration. Although no spectral hydration signatures were found in a subsequent study (Amador et al., 2016).

Little is known about the rare transitioning and bright slope streaks. In this paper, we investigate the properties and plausible origin of these much rarer surface features. First, to find out the extent of bright slope streak distributions and also to locate previously undiscovered transitioning slope streaks, we implemented a grid mapping approach of Arabia Terra using MRO's Context Camera images (CTX; Malin et al., 2007). We then investigated the photometric parameters of these streaks, such as particle size, roughness and surface texture, through multi-angular observations of all three types of slope streaks (i.e. dark, bright and transitioning; Fig. 1). For this purpose we primarily use images taken by the Colour and Stereo Surface Imaging System (CaSSIS; Thomas et al., 2017) onboard the ExoMars Trace Gas Orbiter (TGO), which is able to acquire such multi-angular data due to the non-sun-synchronous orbit of TGO. To investigate particle size effects, we

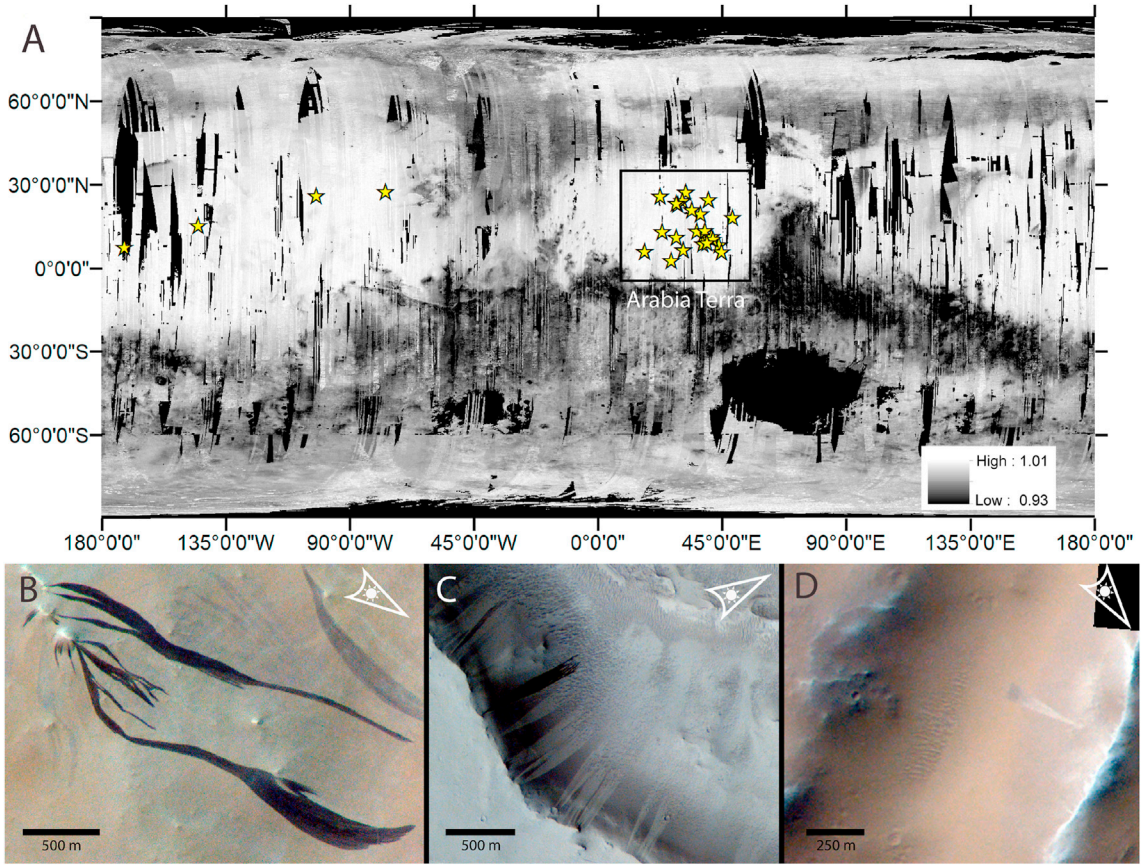

Fig. 1. A) OMEGA derived nanophase ferric oxide spectral parameter map (Ody et al., 2012) overlain with locations studied in this work (yellow stars). Regions of ferric oxide parameter larger than 1 are generally dusty, low in thermal inertia and dominated by fine particles. Regions shaded in black correspond to an absence of data. B) Relatively fresh dark slope streaks on a crater wall in Arabia Terra (site S25). These streaks are observed to flow around obstacles and sustain bifurcating morphology. C) Bright slope streaks on a shadowed slope of a channel in Arabia Terra (S20). The fresher dark slope streak in the middle of the image is capping an older bright streak. D) Transitioning slope streak on a slope of an irregular depression in Arabia Terra (S12). The fan-shaped streak exhibits a contrast reversal partway downslope and was first observed by Sullivan et al. (2001). CaSSIS IDs in respective order: MY35_010269_009_0_RPB, MY34_002312_006_2_RPB and MY35_009517_177_0_NPB. Sun illumination shown in the top right corner of each image. North is up in all panels.

compared our CaSSIS observations with the spectral reflectance of the Mars Global Simulant (MGS-1) soil (Cannon et al., 2019), measured with the PHIRE-2 (PHysikalisches Institut Reflectance Experiment - 2) radio-goniometer (Pommerol et al., 2011) and the Mobile Hyperspectral Imaging System (MoHIS; Pommerol et al., 2015). In addition, we used a reflectance model (Hapke, 2012) to analyze the effects of particle size on the regolith albedo. When higher resolution or a time dependent analysis were found to be necessary (and were available), we complemented the CaSSIS observations with images acquired by HiRISE and MOC.

2. Methods and data

2.1. Mapping of bright slope streaks in Arabia Terra

Based on MOC observations, it was shown that bright slope streaks are more common in Arabia Terra and are much rarer in other geologic regions where dark slope streaks are abundant (Schorghofer et al., 2007). To map the complete regional distributions of bright slope streaks in Arabia Terra we used a normalized global CTX mosaic, which has been

Table 1
Coordinates, IDs, streak category, CaSSIS IDs, atmospheric opacity values, phase angle and date for slope streak sites analyzed in this study.

Long (°E)	Lat (°)	ID	type of streaks	CaSSIS IDs	tau (τ)	phase angle (°)	date, UTC
31.91	27.26	S1	transitioning, bright	MY35_009479_155_0	0.34	24.3	2020-01-07T23:04:24.860
				MY35_013296_153_0	0.48	84.3	2020-11-15T11:55:46.597
				MY35_013582_153_0	1.52	53.2	2020-12-08T21:56:26.811
28.49	11.15	S2	transitioning	MY35_009616_169_0	0.22	9.7	2020-01-19T04:22:24.392
30.62	24.22	S3	bright, dark	MY35_009678_156_0	0.22	33.5	2020-01-24T06:08:13.632
28.94	23.03	S4	transitioning, dark, bright	MY35_008591_024_0	0.13	83.0	2019-10-27T05:19:48.389
				MY35_009417_160_0	0.21	36.5	2020-01-02T21:15:40.619
				MY35_009504_159_0	0.21	21.3	2020-01-10T00:13:29.957
				MY35_013154_026_0	0.37	70.2	2020-11-03T20:10:45.992
38.22	11.74	S5	bright	MY35_010095_012_0	0.19	55.0	2020-02-27T08:48:07.250
35.82	13.38	S6	dark, bright	MY35_010685_170_0	0.47	73.6	2020-04-15T17:05:19.745
38.15	8.81	S7	transitioning, bright, dark	MY35_009653_172_0	0.18	19.6	2020-01-22T05:05:49.535
				MY35_013079_009_0	0.52	56.7	2020-10-28T16:42:57.676
43.86	8.34	S8	transitioning, dark, bright	MY35_010244_008_0	0.26	13.6	2020-03-10T13:35:08.952
				MY35_011823_010_0	1.15	56.5	2020-07-17T20:31:11.423
22.61	25.82	S9	dark, bright	MY35_008410_160_0	0.22	53.7	2019-10-12T10:23:11.700
38.76	13.51	S10	transitioning, dark	MY35_012152_169_0	0.77	50.4	2020-08-13T19:54:47.793
44.76	5.91	S11	transitioning, dark	MY35_012127_175_0	0.82	48.3	2020-08-11T18:49:48.689
16.93	6.03	S12	transitioning	MY35_009517_177_0	0.14	28.4	2020-01-11T01:52:12.008
				MY35_010133_006_0	0.33	44.2	2020-03-01T11:26:41.507
				MY35_010636_177_0	0.28	81.4	2020-04-11T16:50:19.535
257.86	26.01	S13	transitioning, dark	MY35_010187_027_0	0.24	32.2	2020-03-05T21:40:30.724
				MY35_010274_026_0	0.22	17.0	2020-03-13T00:38:22.073
37.16	19.56	S14	dark, bright	MY35_009367_163_0	0.18	53.3	2019-12-29T19:01:25.425
				MY35_009454_163_0	0.16	37.8	2020-01-05T21:59:21.763
40.06	24.62	S15	Transitioning, bright	MY35_009342_158_0	0.13	55.0	2019-12-27T17:52:05.328
				MY35_009429_158_0	0.10	40.0	2020-01-03T20:49:56.666
				MY35_010381_028_0	0.28	31.1	2020-03-21T18:54:44.502
				MY36_015024_154_0	0.14	34.9	2021-04-05T23:39:44.468
				MY36_016143_156_0	0.05	45.8	2021-07-06T14:38:36.754
48.90	18.30	S16	transitioning, dark, bright	MY34_005562_162_0	0.79	37.7	2019-02-21T07:08:41.063
				MY36_014887_165_0	0.03	12.3	2021-03-25T18:29:27.025
				MY36_014974_161_0	0.11	19.6	2021-04-01T21:26:35.254
				MY36_016466_161_0	0.07	32.9	2021-08-02T01:24:03.246
41.23	11.38	S17	bright, dark, transitioning	MY35_010747_172_0	0.37	56.4	2020-04-20T18:56:10.000
41.66	10.41	S18	dark, bright	MY35_007017_173_0	0.38	45.6	2019-06-20T09:02:44.452
				MY35_011207_170_0	0.42	71.6	2020-05-28T10:52:56.892
				MY35_011848_013_0	0.91	73.0	2020-07-19T21:39:46.529
26.66	2.69	S19	transitioning, bright	MY35_007030_182_0	0.28	49.1	2019-06-21T10:38:07.499
				MY35_010257_002_0	0.21	15.2	2020-03-11T15:06:01.004
30.90	6.60	S20	dark, bright	MY34_002312_006_2	0.29	41.8	2018-05-31T06:57:02.000
				MY34_003804_006_2	0.46	52.8	2018-09-30T09:24:06.645
28.50	23.42	S21	transitioning, dark	MY35_010083_024_0	0.33	57.8	2020-02-26T09:17:14.203
33.98	20.88	S22	transitioning, bright	MY35_012930_021_0	0.61	50.5	2020-10-16T11:58:49.048
23.38	13.20	S23	dark	MY35_013179_016_0	0.44	76.2	2020-11-05T21:15:07.097
214.93	15.23	S24	dark	MY36_014844_167_0	0.18	21.8	2021-03-22T06:00:29.909
				MY36_014931_166_0	0.10	7.5	2021-03-29T08:58:22.071
				MY36_015485_014_0	0.03	46.2	2021-05-13T16:49:17.575
39.60	9.19	S25	dark	MY35_010269_009_0	0.17	11.9	2020-03-12T14:43:04.053
				MY36_015049_170_0	0.19	28.0	2021-04-08T00:52:43.664
				MY36_015777_009_1	0.14	42.3	2021-06-06T14:36:11.960
				MY36_015777_009_2	0.14	30.7	2021-06-06T14:36:59.960
282.91	27.49	S26	dark	MY35_006735_152_0	0.27	32.2	2019-05-28T06:59:41.418
188.25	7.56	S27	dark	MY36_014932_173_0	0.16	13.9	2021-03-29T10:58:59.075
				MY36_015019_173_0	0.08	18.6	2021-04-05T13:56:03.446
37.79	11.24	S28	dark, bright	MY36_014875_169_0	0.06	18.2	2021-03-24T18:56:58.832
				MY36_014962_169_0	0.02	5.2	2021-03-31T21:54:02.203
				MY36_016454_169_1	0.04	28.5	2021-08-01T01:51:35.195
				MY36_016454_169_2	0.04	35.1	2021-08-01T01:52:22.195
21.64	12.64	S29	dark, bright	MY36_014975_168_0	0.04	9.1	2021-04-01T23:26:24.259
				MY36_016467_168_1	0.04	35.9	2021-08-02T03:23:57.251
				MY36_016467_168_2	0.04	40.6	2021-08-02T03:24:45.251

recently released by Dickson et al. (2018). It provides an excellent opportunity for large scale surveys of geologic features that are larger than 10 m in size. MRO's CTX acquires panchromatic (500–750 nm) images at 5–6 m/px in resolution, and with image swaths of 30 km x ≥ 40 km, it has imaged >97% of the Martian surface. We selected a 30° × 40° bounding box in Arabia Terra (Fig. 1) and employed a qualitative grid-mapping method (Ramsdale et al., 2017). This region of interest was divided into ~16,000 hexagonal facets 20 km in diameter. 20 km size hexagons were determined to be the most optimal for rapid large scale studies. Each hexagon was assigned a category: 1) no data available, 2) bright slope streaks absent 3) bright slope streaks present. To qualify for the third category at least one bright slope streak had to be present in a hexagon. In addition, to date, only one case of transitioning slope streak had been observed (Sullivan et al., 2001; Baratoux et al., 2006, also see Fig. 1D). Thus, we also use our mapping efforts to search for more transitioning slope streaks in Arabia Terra.

2.2. CaSSIS photometry

Given TGO's non-Sun-synchronous orbit, CaSSIS can monitor surface changes at varying local solar times (LST), several times per Martian season. We made use of this capability by acquiring multi-angular observations of several selected slope streak sites in our study (see Table 1). This allows us to investigate plausible phase-angle-dependent effects, which are closely associated with surface parameters such as particle size, porosity and/or roughness (Fernando et al., 2016). CaSSIS observations are generally acquired in at least two of the four possible color bands (BLU 497 nm, PAN 677 nm, RED 835 nm and NIR 940 nm; Roloff et al., 2017; Perry et al., 2021 this issue). The observations we use in this paper were primarily taken in all four CaSSIS filters. We display them here as NPB (NIR, PAN, BLU) or RPB (RED, PAN, BLU) linearly stretched false color composite products (Perry et al., 2021, this issue). This allows us to investigate possible compositional differences between dark, bright and transitioning slope streaks.

We selected 25 sites in Arabia Terra that contained dark, bright and transitioning slope streaks for the photometric analysis study. Additionally, we include one site in Tharsis, one in Labeatis Fossae and two in Amazonis Planitia (see Table 1 for details). Out of a total of 29 sites, 14 include transitioning slope streaks that had previously never been imaged. The three types of slope streaks observed in our study (see Fig. 1 for examples) are defined as follows: (1) dark slope streaks are entirely darker than their surroundings, i.e. the whole streak, from apex to terminus has a lower apparent brightness in images then the surrounding terrain; (2) bright streaks are entirely brighter than their surroundings from apex to terminus; (3) transitioning streaks are brighter than the surroundings at the apex, but the contrast reverses partway downslope, i.e. the terminus of a transitioning streak is darker than its surroundings. We measured the I/F values of the apexes and termini of selected slope streaks (I/F = detected radiance (I) divided by the solar irradiance at zero incidence (F), such that I/F = 1 for a normally illuminated, perfectly diffuse reflector). To do this, we calculated the mean I/F values of regions-of-interest (ROIs), typically 30–100 pixels in size. The ROI I/F averages (numerator) for each CaSSIS band were then divided by respective I/F values for similar ROIs of the surrounding surface (denominator), which results in ratioed reflectance spectra. Such relative photometry methods are well established (e.g. Daubar et al., 2016; Schaefer et al., 2019; Munaretto et al., 2020, 2021), and afford the advantage of cancelling out the reflectance dependence at the condition that both ROIs selected have the same local slope and aspect. Ratioed reflectance spectra also partially cancel out atmospheric attenuation effects. However, light scattered by the Martian atmosphere is an additive, not a multiplicative term. Also, scattered light is dependent on: 1) wavelength (greater at low BLU than long NIR wavelengths), 2) phase angle (atmospheric column is larger for larger phase angles) and 3) optical opacity (τ) values. While a detailed and quantitative study of these effects is left for future work, we use atmospheric opacity values to qualitatively assess the potential impact of atmospheric effects on the surface reflectance.

A quantitative assessment of the atmospheric conditions in each CaSSIS observation was made using the climatological assimilation of dust opacities derived from the Mars Climate Sounder (MCS) instrument (McCleese et al., 2007). The assimilated MCS column dust optical depths provide a global-scale reanalysis of the atmospheric dust loading during a period of the CaSSIS observations, with a grid point spacing of approximately 200 km. The assimilation is an extension of the Open access to Mars Assimilated Remote Soundings (OpenMARS) dataset (Holmes et al., 2020), a publicly available global record of Martian weather from 1999 onward. The image execution times and location of each CaSSIS image were then used to extract the dust opacity at visible wavelengths, which gives a dust optical depth value to accompany each CaSSIS image. While this approximation provides a means to evaluate whether a CaSSIS image is suitable for color and multispectral analysis, we note that the assimilation is rather coarse in resolution (~200 km × 200 km). Thus, a particular opacity estimate may not reflect the conditions under which a particular CaSSIS image (generally less than 10 × 50 km on average) was taken, and is only used as a proxy for a more accurate estimation of dust opacity.

2.3. Laboratory measurements

Precise, image-based photometric analyses of the Martian surface are often complicated by differences in illumination and observation geometries among images, varying amounts of scattering by aerosols and clouds in the atmosphere, or the limited signal-to-noise ratio of the data. Such studies are therefore ideally complemented by measurements of the reflectance of analogs in the laboratory and physical modelling of light scattering. Physical modelling allows us to vary all relevant parameters independently within a wide parameter space, in order to investigate their influence and understand the physical causes behind photometric behaviors. On the other hand, experimenting with actual analogue soil samples allows us to consider some of the complexity encountered on real planetary surfaces (including possible correlations between the parameters), and can provide ground truth for the interpretation of remote-sensing data. Here, we use both approaches in a complementary way.

For decades, JSC Mars-1, a natural weathered volcanic ash from Hawaii (Allen et al., 1998), has been the most widely used Martian soil analogue. It has been used to study on Earth various properties expected to be similar to those of the Martian surface material. JSC Mars-1 is not distributed anymore, however and a replacement is desirable. The CLASS Exolith Lab, located at the University of Central Florida, has undertaken the development of suitable analogous materials for the surfaces of various Solar System objects. There the analogue material is produced by mixing a series of individual mineral and phase components based on our knowledge to date of the compositional characteristics of soils (Cannon et al., 2019). In particular, their Mars Global simulant (MGS-1) was designed to mimic the chemical and mineralogical compositions of soil from the Rocknest site, which was analyzed by Curiosity (Blake et al., 2013) and considered the best characterized Martian soil to date. Note however that the composition of this soil sample is nearly indistinguishable from that of other in-situ soil samples, which is what makes it suitable as a global soil simulant that can be used in a variety of contexts. The overall composition of the sample is basaltic, but it also contains hydrated silica, ferrihydrite and magnesium sulfate to simulate the amorphous fraction of the Rocknest sample, which itself consists mainly of basaltic glass with amorphous or poorly crystalline components derived from Martian dust.

To prepare our MGS-1 sample for analysis, we baked it at 333 K for 24 h and then dry-sieved it using a sonic separator (VariSifter™ from Advantech Manufacturing, Inc.) to retrieve the different size fractions we investigated (Fig. 2). Note that because of the way the initial sample was produced (i.e., mixing several components with different particle size distributions and resistance to crushing), dry-sieving the bulk sample

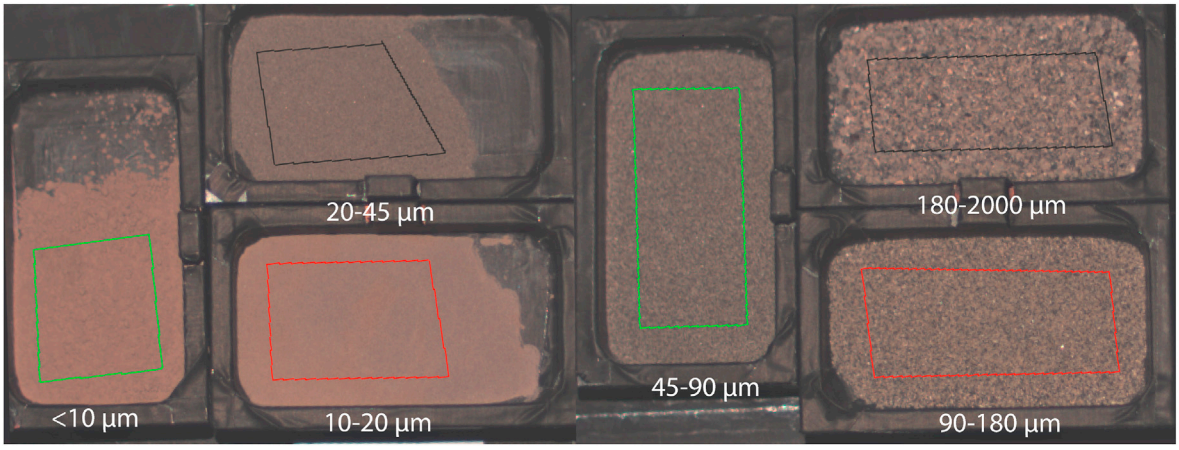

Fig. 2. Spectral image of sieved MGS-1 sub-samples of different size fractions in measurement containers. Colored bounding boxes represent the regions of interest (ROI) that were used for the spectral measurements.

almost certainly results in some mechanical fractionation of minerals/phases between the different particle size fractions. However, such fractionation is also expected on Mars, where the bimodal distribution of particle sizes corresponds to a mineralogical distinction between fine dust particles rich in iron oxides and coarser sand-sized particles derived from local mechanical alteration of the basaltic crust. Based on this assumption, we use the smallest particle size ranges of sieved MGS-1 samples to serve as an analog for the surface fine grains found in slope streak rich equatorial regions. However, such analog samples should be used with caution since the dust grains present in bright and low thermal inertia regions of Arabia Terra are not well constrained and have not been studied in detail by any lander.

The resulting size-sorted samples were then characterized using different techniques, including visible (VIS) Bidirectional Reflectance Distribution Function (BRDF), and visible and near-infrared (VIS-NIR) hyperspectral imaging. To experimentally test phase angle effects on reflectance behavior of sieved MGS-1 samples, we used the PHIRE-2 radio-goniometer. PHIRE-2 is designed to measure the visible bidirectional reflectance of surface samples over a wide range of geometries and under cold (240 K) to ambient (295 K) conditions (Pommerol et al., 2011). Two mobile arms rotate around the samples within a hemisphere to illuminate the sample and measure the scattered radiance within a wavelength range restricted by one of six bandpass filters (with centers at 450, 550, 650, 750, 905 and 1064 nm and with Full width at Half Maximum bandpasses of 70 nm for VIS wavelengths and 30 nm for NIR wavelengths). The measurements are automated to produce dense sets of reflectance data, which can then be interpolated and integrated to estimate the hemispherical albedo of the sample or other photometric quantities, or fit by photometric models. The reflectance data are radiometrically calibrated by comparing the measurements of the sample to measurements of a plate of Spectralon™ (Labsphere) that has well-known reflectance properties.

For each particle size fraction of MGS-1 we also acquire high resolution spectra using The Mobile Hyperspectral Imaging System (MoHIS). MoHIS was constructed from the setup previously used to acquire hyperspectral images of samples in the Simulation Chamber for Imaging the Temporal Evolution of Analogue Samples (SCITEAS; Pommerol et al., 2015). MoHIS consists of two cameras, one sensitive in the VIS range (0.4–1.0 μm) and the other in the NIR (0.9–2.4 μm), and a monochromatic illumination system, allowing acquisitions of hyperspectral images of the samples (Pommerol et al., 2015). The hyperspectral cubes are produced by illuminating the sample with monochromatic light, and then acquiring an image with one of the two cameras before shifting the wavelength slightly and repeating the procedure. We acquire these measurements with high spectral resolution (6.5–13 nm), and a spectral sampling such that there is overlap between adjacent bands (6–15 nm), mimicking datasets acquired by orbital instruments such as OMEGA or CRISM. From the hyperspectral cubes, averaged spectra over user-defined regions of interest (ROI) can be calculated and exported. As with PHIRE-2, the radiometric calibration of the MoHIS data consists of a normalization to the measured reflectance of a Spectralon™ plate after subtraction of a dark signal (see Pommerol et al., 2015; Yoldi et al., 2021) and correction of minor absorption by the Spectralon beyond 2 μm using manufacturer data.

2.4. Reflectance modeling

To complement orbital observations and laboratory measurements in this work, we used the Hapke spectral reflectance model (Hapke, 2012) (for methodology see the Appendix section). Our goal was to investigate the effects of different particle sizes of Martian dust on the spectral reflectance that would be observed by orbital imagers. Our implementation of the model primarily follows the approach of Becerra et al. (2015), which is itself based on those of Roush (1994) and Warell and Davidsson (2010), and neglects atmospheric extinction and scattering. The model simulates the reflectance spectra of a uniform dusty surface on Mars for a user-given mean particle size with a 1 nm spectral sampling between 300 and 4000 nm. The complex indices of refraction (optical constants) of the simulated dust are obtained from the CRISM/OMEGA measurements of Wolff et al. (2009). In order to simulate instrument observations, the 1 nm model spectra are convolved with the instrument bandpasses. Convolving the raw modeled spectra with the CaSSIS band-pass coefficients (Thomas et al., 2017) results in simulated CaSSIS I/F values for each grain size selected. The same convolution procedure was also used to convolve the MoHIS measurements to CaSSIS I/F, outputting laboratory-based simulations of CaSSIS observations of the MGS-1 simulant.

3. Results

3.1. Mapping of bright slope streaks in Arabia Terra

The results of our grid mapping campaign are shown in Fig. 3. The region of interest is roughly 2000 km × 2000 km in size and covers most of Arabia Terra where bright slope streaks exist. An initial observation at this scale suggests that bright slope streaks are very common in Arabia Terra. The distribution of bright slope streaks in our study area is not homogeneous, i.e. the density of the streaks increases towards the center of the map. We note that an HRSC-MOLA slope mosaic does not suggest steep slopes in these regions. Moreover, the crater size-frequency distributions do not appear to be correlated with the increased density of bright slope streaks, although some bright streaks are observed around

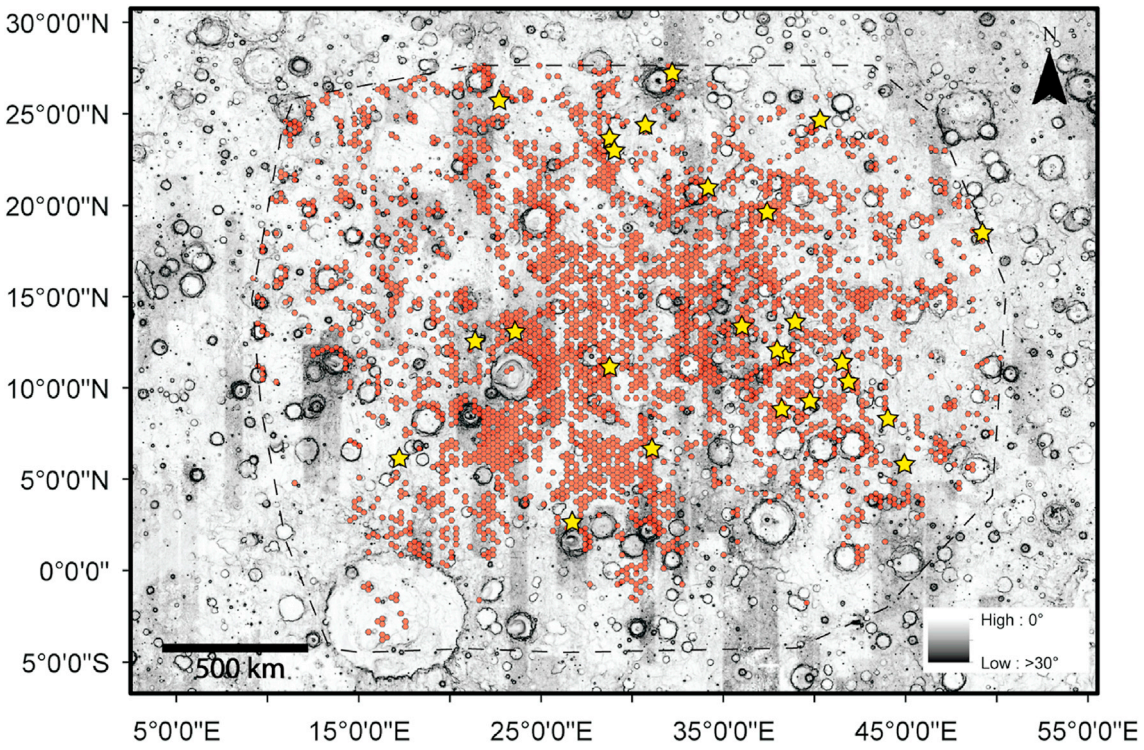

Fig. 3. Bright slope streak distribution in Arabia Terra (red hexagons) based on mapping with a global 5 m/px CTX mosaic (Dickson et al., 2018). Each shaded hexagon (20 km in size) indicates at least one bright slope streak present in that area (see Ramsdale et al. (2017) for grid-mapping methodology). Yellow stars indicate locations of CaSSIS multi-angular color photometry. The basemap is HRSC-MOLA slope mosaic (200 m/px).

the rims of large craters. At smaller local scales not resolvable by this map, streaks are primarily found around small craters, channels and hills. An OMEGA nanophase ferric iron oxide abundance map (300 m/px to 5 km/px) (Ody et al., 2012) and TES dust cover index map (3.5 km/px) (Ruff and Christensen, 2002) indicate evenly distributed dust in this region. The bright slope streak distributions are likely correlated with regions where dark slope streaks are less active, i.e. regions with few fresh dark streaks contain many old bright slope streaks (see also Schorghofer et al., 2007). Alternatively, there could be a regional thicker settled dust layer in the center of Arabia. However, the apparent lack of bright streaks in other regions than Arabia may suggest different surface fines particle size distribution and/or composition.

3.2. Observation of a brightening slope streak

A time-dependent slope streak contrast reversal that would provide clues about the relationship between dark and bright streaks, has not yet been reported. Here, we have captured such a contrast reversal of several slope streaks at one site in our study region within Arabia Terra (site S15; Fig. 4). This site was first observed at high resolution by MOC, on 2001-04-16, and the streaks visible in this MOC image appear dark, although slight brightening at the apexes can already be observed. On 2019-12-27, CaSSIS observed this site again, with a slightly different Sun-azimuth direction (incidence: 56.5°) as the original MOC observation (incidence: 35.6°). The streaks in this CaSSIS image appear almost completely bright.

Finally, the same location was observed recently by HiRISE on 2020-10-04, which confirmed the observation in the CaSSIS image, i.e. that such streaks are indeed brighter than their surroundings. These three observations by MOC, CaSSIS and HiRISE suggest an apex-to-bottom brightening process. To rule out possible photometric effects, i.e. the prospect that streaks appear brighter under high phase angle illumination, we present multi-angular observations that show on the contrary that streaks brighten with decreasing phase angle (see subsection 3.4).

3.3. Slope streak color observations

Based on photometric measurements of 34 dark, 25 bright and 19 transitioning streaks from all our study sites, we calculated ratioed reflectance spectra in each CaSSIS band (Fig. 5). Averages were based only on images that were identified by the atmospheric model to have $\tau < 1$ (see Table 1). Where more than one observation was available for a given site, only the one with the best atmospheric conditions was included in the average. In total 29 CaSSIS images were used for the calculation of ratioed reflectance averages. For each streak we included one measurement at the apex and one at the terminus, which revealed that on average all 3 types of streaks are brighter at the apex and darker at the terminus. Dark streaks are on average darker than their surroundings by ~6% and bright streaks are brighter by ~2%. The darkest streak was found to be 12% darker and the brightest streak 4% brighter than the surroundings. The largest difference between apex and terminus measurements can be seen in transitioning slope streak spectra, for which the apex is brighter than the terminus by about 3%. We also observed that both transitioning streak termini and both sections of dark slope streaks exhibit a characteristic "kink" upwards from PAN to BLU wavelengths. CRISM spectral ratios of dark slope streaks exhibited the same spectral kink at <500 nm (Mushkin et al., 2010). Lastly, bright streaks and the apex of transitioning streaks instead display a roughly flat spectrum, indicative of no difference in particle size.

3.4. Slope streak multi-angular observations

Phase angle dependent phenomena related to particulate materials are known to occur on Mars. For example, dark sand deposits in Juventae Chasma appeared brighter than their surrounding in high phase angle images, thereby suggesting that it is comprised of strongly forward-scattering material (Geissler, 1992; Johnson et al., 2008). To investigate how the reflectance of bright and transitioning slope streaks varies with phase angle, we imaged site S1 (Fig. 6) under three different

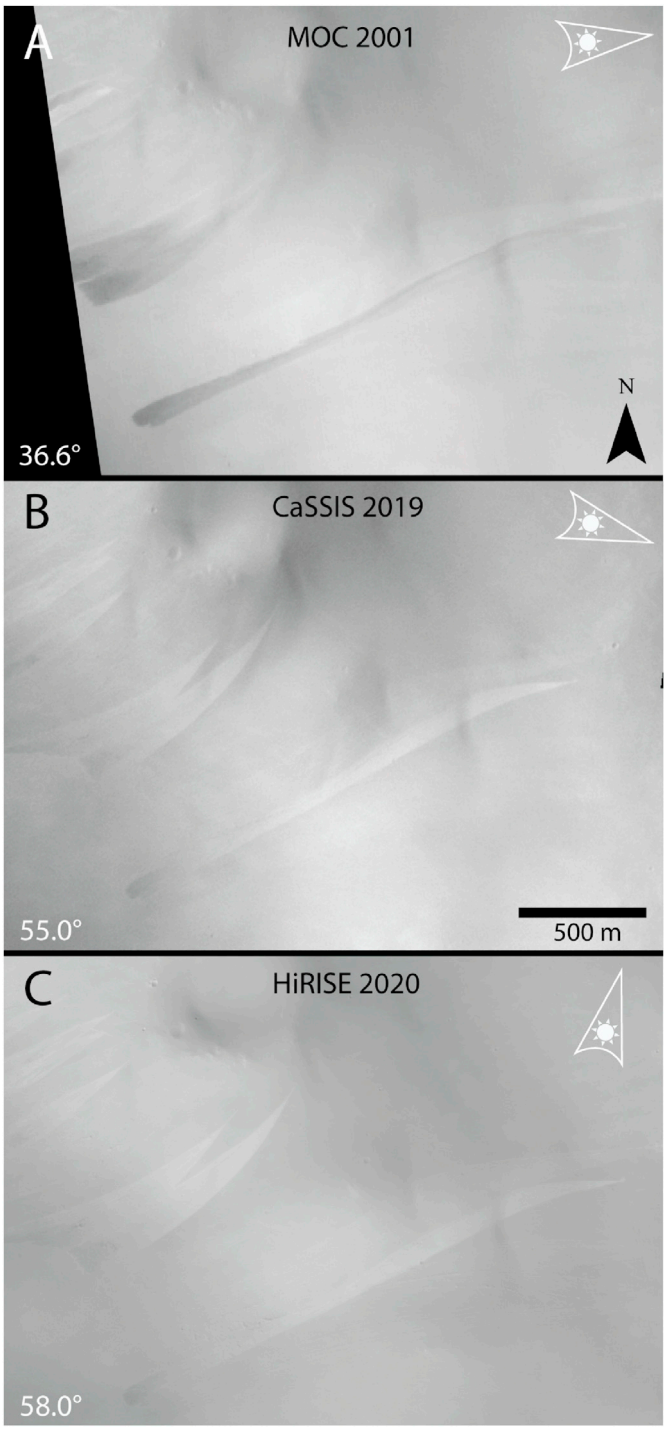

Fig. 4. Time-lapse image sequence of slope streaks, exhibiting a contrast transition from dark into bright relative to the surrounding terrain. (A) MOC observation E0301436 taken on 2001-04-16. (B) CaSSIS PAN image MY35_009342_158_0 taken on 2019-12-27. (C) HiRISE RED image ESP_066514_2050 taken on 2020-10-04. The phase angles are shown at the bottom left of each panel. Sun illumination direction shown in the top right of each image.

illumination geometries. This site includes a transitioning streak and several bright slope streaks. There is a faded bright streak at NW position from the transitioning streak T1, which has almost completely faded into the background (Fig. 6D white arrow). We performed multi-angular photometric measurements on T1 and B1 to understand how ratioed reflectance varies with phase angle. Fig. 6 reveals that differences in brightness of the B1a and B1b sections are phase-angle-dependent. Both apex and terminus measurements show an increase in brightness by 3% in the low phase angle observation (24.3°). T1a also exhibits a similar brightening under low phase. The spectrum of T1b does not exhibit a large dependence on phase angle but the characteristic "kink" from PAN to BLU was observed as in Fig. 5. Optical opacity estimates indicated that τ is 1.523 for the observation shown in Fig. 6B. However, the actual atmospheric conditions for this image appear to be better than those derived from the climatology data.

At site S16 (Fig. 7), which is located in the center of a large crater in Arabia Terra, we acquired three low phase angle observations (12.3°, 19.6° and 37.7°). We analyzed the termini section of two bright streaks (B1 and B2), two dark streaks (D1 and D2) and one transitioning (T1) streak to further quantify changes in brightness. Only the termini parts were selected since they were close to homogeneous dusty areas on a comparable slope (yellowish tone material as seen in the CaSSIS NPB products). The steeper slopes of these outcrops are likely composed of different material and/or dust than the floor unit of this crater. In site S16 we also observed transitioning streaks that are not bright at the apex even in low phase angle observations (see Fig. 7B black arrow). Only surface texture observable in high resolution HiRISE images reveal that the apex is part of the same streak (ID: ESP_060342_1985). A similar type of streak can be also observed in site S21 (Table 1). Fig. 7D shows that several surface details are not visible without high signal-to-noise ratio and good atmospheric conditions. These data points are therefore not included in the photometric analysis.

The results in Fig. 7 show a slight brightening with decreasing phase angle of the two (B1 and B2) bright slope streaks by 1%. However, there is not much difference between the measurements at 12.3° and 19.6°. We again observe here a similar featureless brightening as in Fig. 6. Dark streaks (D1 and D2) also show a sharp ratio decrease by 3% in the BLU, which is even stronger under the lowest phase angle acquisition. The terminus part of T1 presents a flatter spectrum, than that in D1 and D2, but the kink from BLU to PAN is still recognizable within about 2%. The last plot in Fig. 7 features the ratio of the termini parts of transitioning (T2) and bright (B3) slope streak. The T2/B3 ratio at 19.6° phase is lower than at 37.7° phase likely because the bright streak terminus (denominator) brightened more than the dark streak terminus (numerator). Also, it illustrates that the spectral ratio between dark and bright streak is comparable in shape to that of dark slope streak and surrounding dust (i.e. the same kink in D1, D2 and T1 plots).

We summarize our CaSSIS multi-angular results for bright and dark slope streaks in Fig. 8. This plot, in the CaSSIS PAN band (677 nm), is based on measurements of all sites from Table 1 that include two or more images and have at least one under 20° phase. Each site on the plot is a separate curve composed of either individual images and/or stereo observations. Dark slope streaks, in comparison to bright ones, exhibit a steeper phase slope and in some cases brighten by up to ~7% (site S24, 7.5–46.2° phase). Bright streaks show a slight (up to 1%) brightening with decreasing phase and in some cases even no brightening at all (see nearly flat spectra of site S7, 19.6–56.7° phase). A difference in reflectance can also be observed between stereo pairs (data points marked as stars), where the lower phase observation always includes larger ratioed reflectance value. Since CaSSIS stereo pairs are acquired roughly within 40 s, the atmospheric column in both images should be the same, therefore the observed signal is due to the light scattering properties of the surface. Fig. 8 illustrates that with decreasing phase angle dark streaks brighten more, relative to the surrounding terrain, than do the bright streaks. Also, based on this plot, we do not observe the hypothesized slope streak contrast reversal inferred from observations of Earth snow avalanches (Baratoux et al., 2006). Additionally, we have investigated the other three CaSSIS filters but did not observe a considerable wavelength dependence. However, in the BLU filter dark streaks exhibited slightly bluer ratioed reflectance values (shifted upwards in the y-axis) but retained the same slope and phase dependence. This conclusion generally agrees with multi-angular observations of OMEGA and

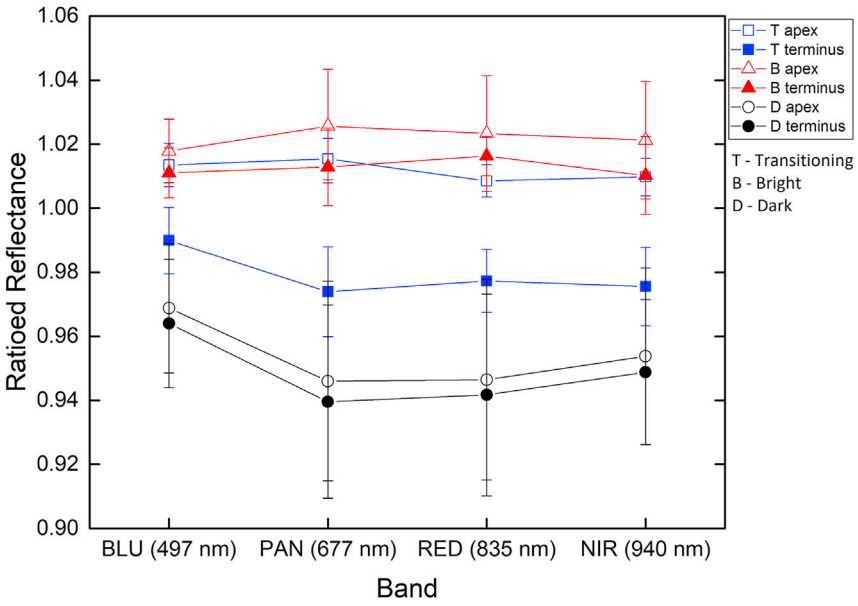

Fig. 5. Average ratioed reflectance plot in the four color bands of CaSSIS (BLU, PAN, RED and NIR) for 34 dark, 25 bright and 19 transitioning slope streaks analyzed in this work. The bright streak and transitioning streak apex section spectra exhibit a featureless brightening. For both sections of dark streaks and transitioning streaks terminus part, the measurements show a decrease from the BLU (497 nm) to PAN (677 nm) ratioed values. Errors bars are 1 sigma and suggest that a large variety of slope streak contrast states exist.

CRISM (Vincendon, 2013) that indicated that Mars' surface phase function behavior is independent of wavelength, at least for some surface materials.

3.5. Laboratory measurements and comparison to CaSSIS data

The results of multi-angular measurements using the PHIRE-2 radiogoniometer for six grain size fractions of MGS-1 (at wavelengths 450, 650 and 905 nm) are shown in Fig. 9, together with their reflectance spectra for the same grain size fractions acquired by MoHIS. From multi-angular data we can observe that for all particle phase curves, reflectance starts to increase as the phase angles approach low values. The latter behavior is expected for particulate materials and is characterized by an exponential increase in reflectance towards 0° phase. This phenomena is known as the opposition surge effect and is composed of two components: 1) the shadow hiding effect due to decreasing shadows between the particles as opposition is approached (Hapke, 1984; Shkuratov et al., 1994; Shkuratov and Helfenstein, 2001), and 2) the coherent backscattering due to constructive interference of photons at very small phase angles (Muinonen, 1994; Muinonen et al., 2010). Depending on the material, the coherent backscattering peak can be very narrow (~<2°), whereas the shadow hiding peak is relatively broad (~<20°) (e.g. Helfenstein et al., 1997). Therefore, since most of our CaSSIS data are above the phase angle range where coherent backscattering occurs, it is likely that our observations in Fig. 8 illustrate the increased backscattering due to shadow hiding effects.

To test our hypothesis that slope streaks are composed of larger particles than the surrounding dusty terrains, we calculated the ratio of selected CaSSIS-convolved spectra of the large particles (numerator) to that of MGS-1 with smaller mean particles (denominator). Three selected laboratory ratios for different particle size ranges are shown in Fig. 10. On the same plot we compare these ratioed laboratory spectra with CaSSIS ratioed reflectance spectra of dark and bright streaks from Fig. 5.

We were able to replicate the shape of the dark slope streak spectral ratio using laboratory MGS-1 20-10 and 10-0 μm, 45-20 and 10-0 μm, and 45-20 and 20-10 μm spectral ratios. The characteristic "kink" visible from PAN to BLU band for dark slope streaks resembles the shape of all three MGS-1 ratios at the same wavelength. However, laboratory spectra exhibit a more enhanced and deeper spectral ratio. This could be due to the fact that particles within slope streaks have much broader size distributions than fractions isolated in the lab. We cannot exclude that the PAN to BLU feature of dark slope streak spectra is diminished by atmospheric effects and therefore is more pronounced in the lab spectral ratios. We also cannot rule out the possibility that this feature contains a compositional component (Viviano-Beck et al., 2014).

3.6. Reflectance modeling

The Hapke-modeled reflectance of different particle size fractions of Martian dust are shown in Fig. 11. Our modeling suggests that only a narrow particle size range of relatively small mean grain sizes can reproduce the different reflectance behavior at wavelengths below 500 nm. Indeed, only for mean particle sizes below 20 μm, the spectra diverge from a flat curve with a value of 0.03 Lambert albedo at these wavelengths. This conclusion partially supports our laboratory findings that the only size fractions capable of producing these effects are relatively small particles. Also, the shape of the spectrum of the smallest particle size range and its albedo value generally agrees with the results of Martian dust analog studies (Wells et al., 1984).

4. Discussion

CaSSIS color spectral ratios of dark, bright and transitioning slope streaks suggest a genetic relationship between these three populations. For example, the average ratioed reflectance plot shown in Fig. 5 indicates that the spectra of the dark slope streaks are similar to that of the termini spectra of the transitioning streaks. The spectra of bright streaks also appear to have a similar flat shape to that of the apex of the transitioning streak. This implies that some streaks may form as dark, then enter a transitioning phase, and finally become completely bright. Furthermore, based on Fig. 5, dark slope streak apexes are fainter than their termini, which might indicate a top-to-bottom fading process. In support of the aforementioned evidences, MOC, CaSSIS and HiRISE consecutive observations (Fig. 4) of the site S15 identified a complete dark to bright slope streak reversal. This observation, combined with the CaSSIS spectral evidence, supports the hypothesis that bright streaks may be purely old dark slope streaks (Schorghofer et al., 2007).

Dust deposition might play a role, not only in the fading of slope streaks (Aharonson et al., 2003), but also in their time-dependent brightening. We present a conceptual model, primarily based on dust deposition on pre-existing surface microtexture and its temporal compaction (see Model 1, Fig. 12). Although there are documented cases of slope streaks which contain discernible meter-scale topography, e.g. longitudinal ridges (Chuang et al., 2007; Beyer et al., 2008) and linear mounds (Phillips et al.,

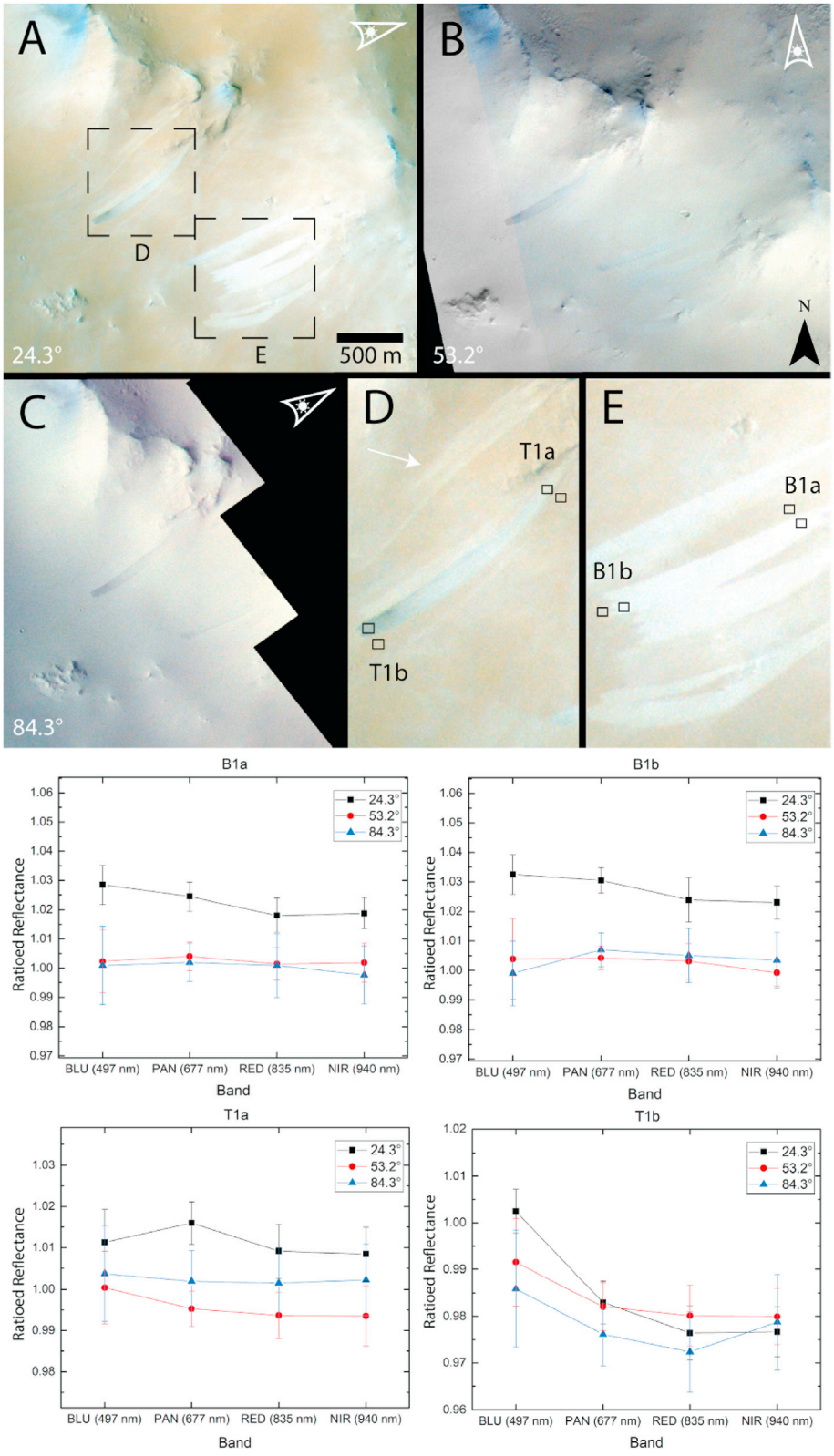

Fig. 6. (A–C) CaSSIS multi-angular observations of site S1 (31.91E, 27.26N), which features a transitioning streak and many bright streaks. (D–E) ROI close ups selected for relative photometry on the transitioning streak (T1a and T1b) and on a bright streak (B1a and B1b). Although the third observation (C) was acquired in low light conditions, the SNR is high enough to obtain reliable photometric measurements. CaSSIS multi-angular ratioed reflectance plots for the apex (B1a) and terminus (B1b) of one bright slope streak and the same measurement for a transitioning slope streak (T1a and T1b respectively). A general brightening with phase is observed for all slope streaks. Bright slope streaks show a featureless brightening in all 4 CaSSIS bands. The terminus part of transitioning streak (T1b) show a sharp decrease in ratio at the BLU band (497 nm). Phase angles are shown on the bottom left (A–C).

2007), in all of our analyzed sites we did not observe albedo contrast dependency on topography. Meter-scale topographic features were observed for both dark, bright and faded streaks alike (e.g. HiRISE ID: ESP_066514_2050). Therefore, we must assume that slope streak photometric darkening/brightening is due to the changes in the surface cm-mm scale microstructure (≪ HiRISE resolution). Model 1 describes a scenario where as the streak forms, it exposes a deeper and darker substrate. Such a substrate would be composed of larger particles than the nearby dusty terrains. Alternatively, a larger particle layer could be achieved due to particle sorting (Kleinhans, 2004), since in granular materials large particles are observed to move to least shear strain zones (Bagnold, 1954). The decrease in reflectance may also be due to the increase in porosity and

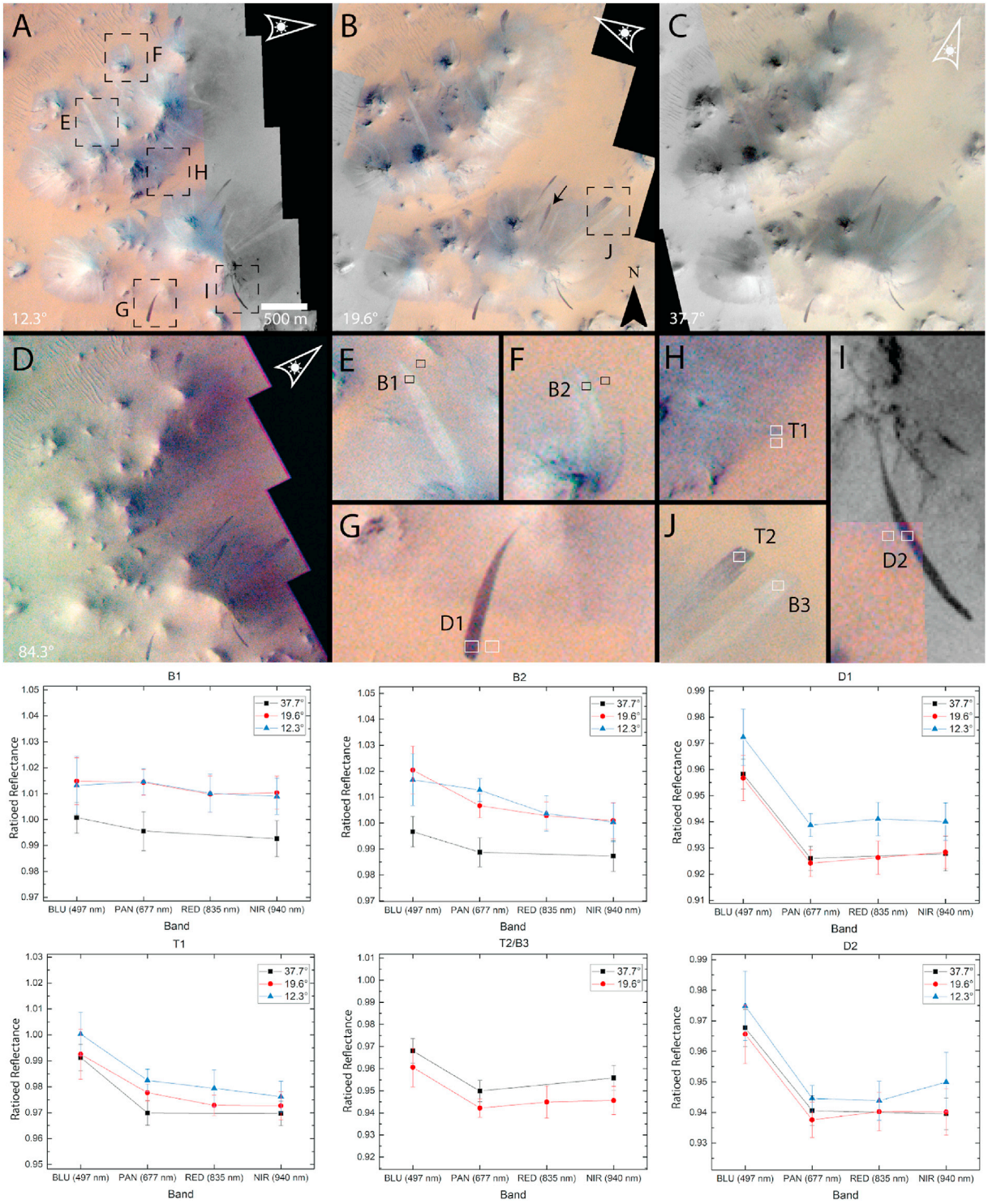

Fig. 7. (A–D) CaSSIS multi-angular observations of various slope streaks for site S16. (E–I) ROI close ups selected for relative photometry (B1, B2, T1, D1 and D2). No photometric analysis was performed on (D), it is only shown here to display the importance of high SNR and good atmospheric conditions in identifying slope streaks. CaSSIS multi-angular ratioed reflectance plots for the terminus of bright (B1 and B2), dark (D1 and D2) and transitioning (T1) streaks at site S16. Ratio plot (T2/B3) of transitioning talus (T2) and bright talus (B3) streak also provided. A general brightening with decreasing phase is observed on all slope streaks. The dark streaks (D1 and D2) and the transitioning streak (T1) show a sharp decrease in ratio at the CaSSIS BLU band (497 nm). A similar effect can be seen in transitioning (T2) and bright streak (B3) termini ratio plot (T2/B3). Phase angles are shown on the bottom left (A–D).

microscopic roughness (Shepard and Helfenstein, 2007). With time, dust would settle on the rough slope streak surface, creating an optically opaque coating and effectively erasing the spectral signature described earlier (i.e. "kink" from PAN to BLU). Perhaps due to particle settling and/or surface properties that allow compaction of dust (Herkenhoff et al., 2004), slope streak reversal in contrast could be achieved. Given enough time, even more dust would settle and fully bury the intricate microstructure. From a spectral perspective, such a surface would be indistinguishable

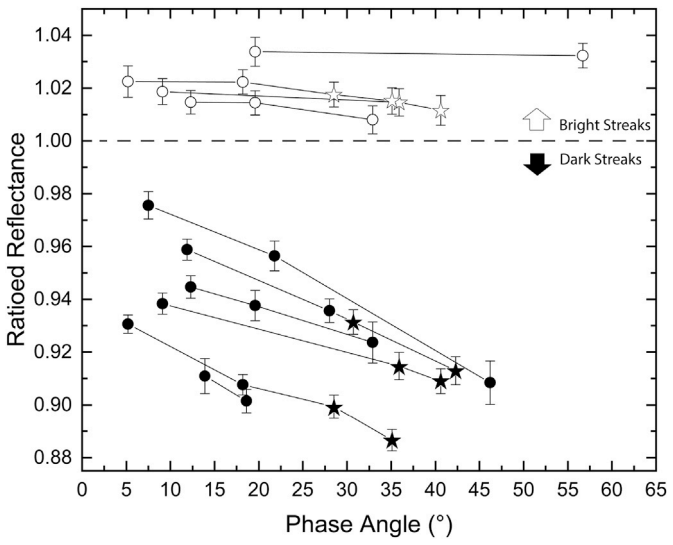

Fig. 8. Multi-angular ratioed reflectance plot in the CaSSIS PAN (677 nm) band, for dark (black dots) and bright (white dots) slope streaks observed in this study. Each set of lines is a different site composed of either individual images (dots) and/or stereo observations (stars). A steep linear phase angle dependency is observed for dark slope streaks likely due to interparticle shadow hiding opposition effect. It suggests that slope streak surfaces are more porous and rough relative to the surrounding terrains. Bright streaks exhibit either no change in brightness or a slight brightening in a few cases, which may indicate that their surfaces are more compact relative to the surrounding materials.

from the nearby terrains. Note that in this model the settled amount of dust is insufficient in erasing macroscopic topography, which may remain intact after the initial avalanche flow.

Although conceptually viable, the described dustfall model, would need to be very slow (on the order of decades) to be consistent with known slope streak brightening/fading rates (Bergonio et al., 2013, also Fig. 4). On Mars most surface features are suggested to fade from atmospheric dust settling relatively quickly. Global changes in surface albedo and therefore dust deposition are known to be modulated seasonally (Szwast et al., 2006). The formation of mesoscale windstreaks was shown to be enhanced during seasons of increased local dust storm activity (Thomas et al., 2003). On a much smaller scale, dust devil tracks, which are formed via dust deflation by moving dust devils, also usually fade within a Martian season (Malin and Edgett, 2001; Balme et al., 2003). Deposition of perhaps a few microns of airfall dust was suggested to be enough to cause dust devil track disappearance (Malin and Edgett, 2001). Also, some dust devils tracks were shown to completely disappear right after global dust storms (Greeley et al., 2010). Interestingly, in case of slope streaks in Lycus Sulci, it appeared that the dust storm in 2001 did not cause them to fade away (Bergonio et al., 2013).

Secondly, Recurring Slope Lineae (RSL) found on equatorial slopes are known to fade seasonally (McEwen et al., 2011; Stillman et al., 2017; Vincendon et al., 2019). Their occurrence on steep slopes around the angle of repose for granular material suggested that RSL may be flows of sand, which remove a thin coating of dust (Dundas, 2020a). Schaefer et al. (2019) proposed that one of the key differences between the fading mechanisms of RSL and slope streaks is their occurrence in two distinctly different albedo regimes. RSL are found in host terrains of albedo <0.1 and slope streaks in that of ~ 0.3 (McEwen et al., 2014). Since low albedo terrains brighten more easily by even small amounts of dust fallout (Wells et al., 1984), Schaefer et al. (2019) suggested that it takes more time for slope streaks to fade from dust deposition. However, it has been noted that dust devil tracks found within the same location as slope streaks, still faded within a few martian seasons, while slope streaks did not appear to be affected (Schorghofer and King, 2011). Paradoxically, high albedo regions like Arabia, which are known to be dusty (Ruff and Christensen, 2002; Szwast et al., 2006) should naturally experience higher dustfall rates, consequently making slope streaks more susceptible to fading by atmospheric dust fallout.

Slope streaks represent a unique type of albedo features that persist for decades on the martian surface. Perhaps the atmospheric dust settling process plays only a minor role and merely provides the raw materials for soil cohesion during the slope streak formation. Therefore, it is conceivable that another mechanism is responsible for slope streak fading and/or brightening. In Fig. 12 we present Model 2 that evokes temporal surface evolution from other factors unrelated to dust fallout. In this model, the assumption that slope streaks expose a darker substrate is also not required. This is evoked in order to be consistent with the observations where boulder tracks on the same slopes as dark streaks do not expose a darker substrate (Mushkin et al., 2010) and the lack of scars in some new streaks (Kreslavsky and Head, 2009). Instead, the flow as it moves downslope consumes and effectively enlarges surficial particles sizes by either: 1) cementation and electrostatic cohesion by weakly bound van der Waals forces (Bridges et al., 2010; Vaughan et al., 2010) or 2) a diagenetic process, which increases the grain sizes of pre-existing iron oxide materials by agglomeration (Mushkin et al., 2010). Cohesion of dust likely due to electrostatic charging has been documented by the Spirit rover (Herkenhoff et al., 2006) and also happens in the martian atmosphere (Harrison et al., 2016). In case of diagenesis, Mushkin et al. (2010) argued that FeOx grains not only increase the volume scattering, but also create mm-cm scale roughness within the slope streak surfaces. Regardless of the exact process responsible for particle enlargement, the resultant surface would likely be very porous and rough. At least for materials made of mixed silica sand, thermal conductivity tends to decrease with high porosity and low proportion of fine particles (Ahn and Jung, 2017). Interestingly, Schorghofer et al. (2007) using THEMIS day IR data observed a dark streak that is warmer than nearby slopes and suggested that this is due to a decrease in thermal conductivity. The next stage of Model 2 illustrates a scenario, where with time, the fragile large grain agglomerates would start to break down, perhaps due to external erosion or the wear-off of interparticle forces. As the particle effective size decreases the albedo of such surface would start to increase. Once all uppermost particles have decomposed, the new layer would likely be more compact than the surrounding slightly more porous terrains. Perhaps once this stage is reached, dust deposition may be able to effectively mask the new small particles and erase the bright streak spectral signatures. The proposed soil degradation process could potentially lead to a scar formation (Gerstell et al., 2004; Kreslavsky and Head, 2009) if the initial agglomerated particle layer is thick enough. Lastly, the observed top-to-bottom brightening process might be controlled by slope because larger aggregates are not as stable on sloping surfaces and are more exposed to wind (Sullivan et al., 2008).

5. Conclusions

Based on CaSSIS spectral and multi-angular evidence from ~30 sites, and temporal observations of one location that exhibited a contrast reversal, we show that slope streaks undergo changes in albedo after their formation. Fresh slope streaks are composed of larger particles, contain a rougher and more porous surface layer, and appear ~10% darker than the surrounding terrains. Within decades, a substantial proportion of slope streaks in Arabia Terra likely experiences regolith compaction and a reduction of the upper surface layer in effective particle size. Eventually this process results in streaks, which are brighter by up to 4% than the surrounding particulate materials. Ultimately even these bright slope streaks fade out and lose their spectral signatures. In this case, meter scale topography observable only in high-res imagery would be reminiscent of the old slope streak.

Our global mapping of bright slope streaks revealed that these features are very common in the Arabia Terra region. Although remote sensing observations by other missions suggest that Tharsis and Arabia regions are covered by comparable albedo, it is plausible that the rarity of

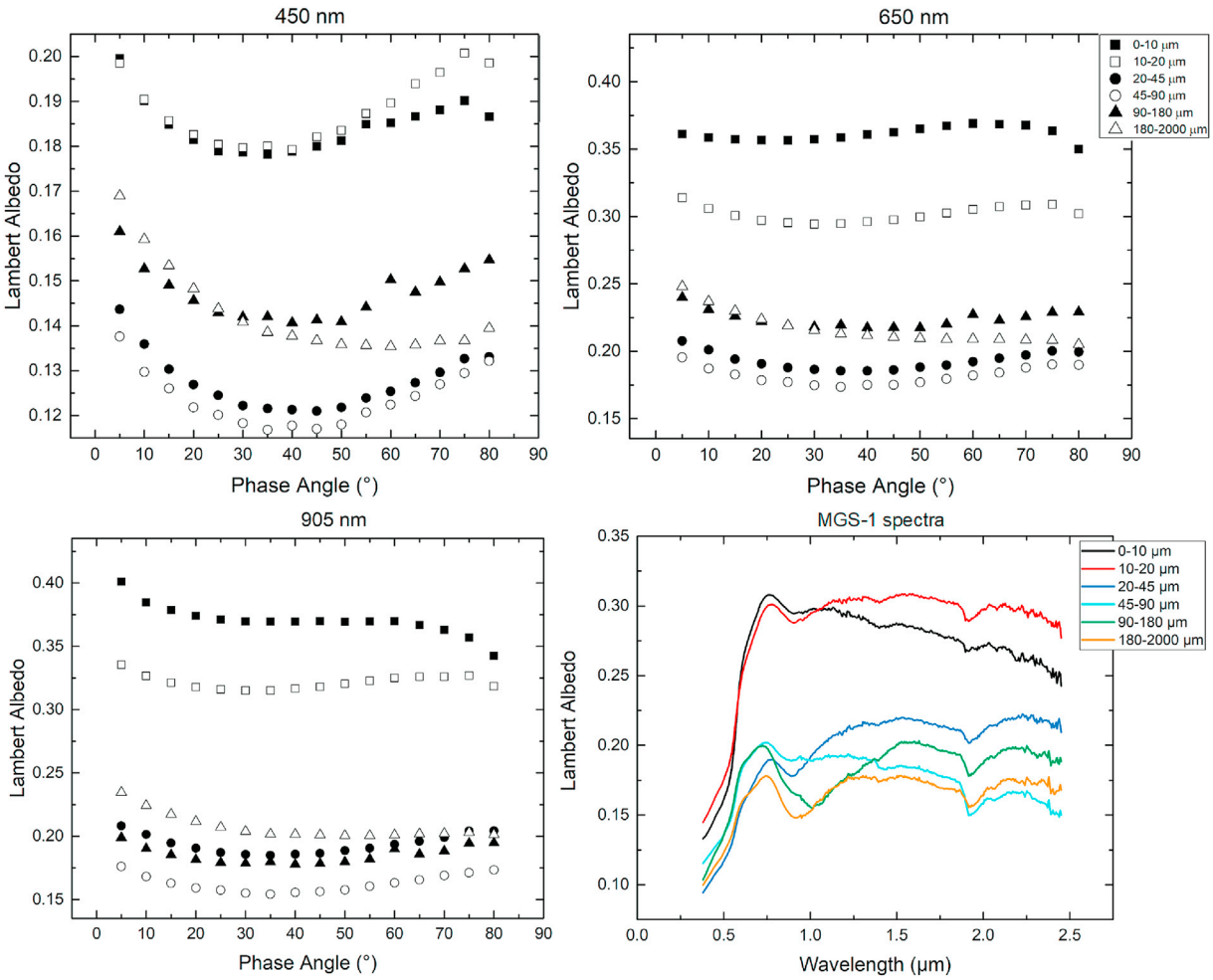

Fig. 9. PHIRE-2 goniometer measurements for all MGS-1 size fractions at three different wavelengths (450, 650 and 905 nm). All grain fractions exhibit increased reflectance as phase angles approach 0°, likely due to the broad backscatterring peak of the shadow hiding effect. The fourth plot features MoHIS acquired spectra for different particle size fractions of MGS-1 sample. The smallest particles exhibit the largest albedo. Spectral range is from 0.38 μm to 2.45 μm. Observation geometry for PHIRE-2 measurements: i = 0°, e = g.

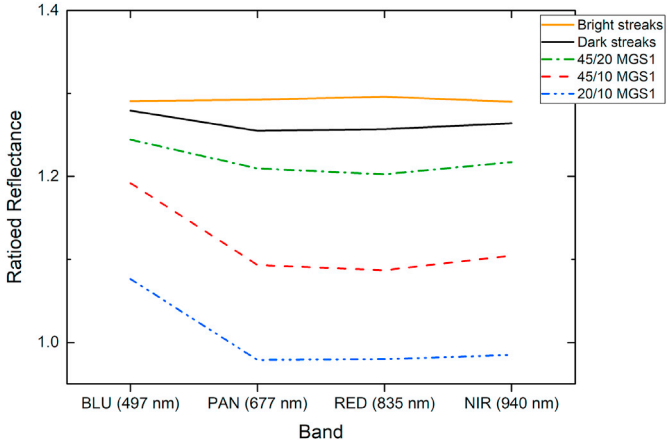

Fig. 10. Ratioed reflectance averages for bright (orange solid line) and dark slope streaks (black solid line), and MoHIS spectrometer MGS-1 CaSSIS convolved spectral ratios for selected particle size fractions. A similar ratio feature can be observed from PAN to BLU for both lab and CaSSIS dark slope streak spectra, which indicates a possible particle size effect. Slope streak spectra taken from Fig. 5. Y axis offset for clarity.

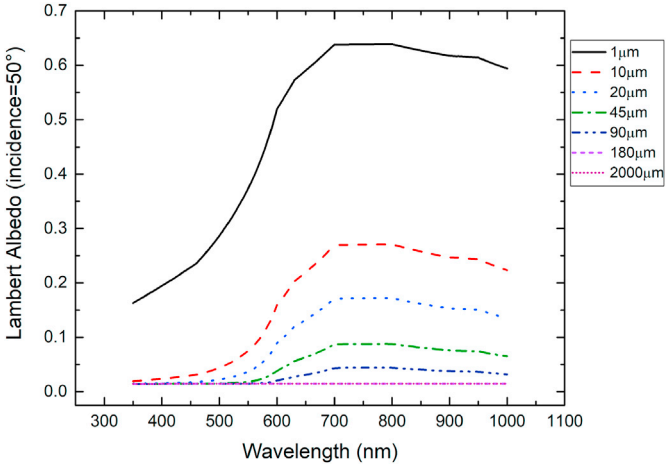

Fig. 11. Modeled Lambert albedo reflectance curves for different grain sizes. The model was run for particle size fractions similar to those analyzed in the lab. The plot illustrates that the smallest particles <10 μm exhibit the largest increase in albedo. The incidence angle was set to equal 50° in order to analyze the reflectance dependence on particle size, unrelated to opposition surge phenomena. Based on optical constants derived from CRISM/OMEGA measurements (Wolff et al., 2009).

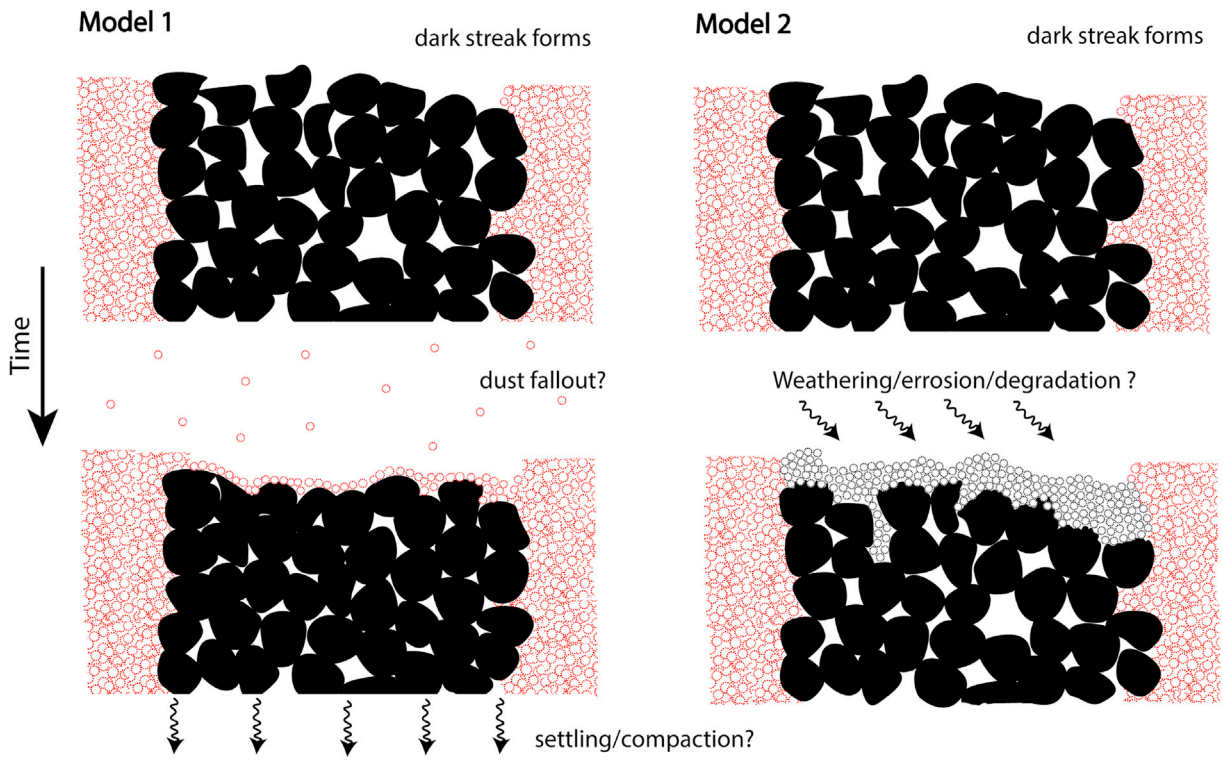

Fig. 12. Surface profile view for two types of slope streak brightening models. Conceptual model of dust fallout (Model 1) and the brightening by decomposition of surface agglomerates (Model 2). In Model 1 the slope streak brightening is achieved by deposition of dust and compaction of the rough larger particle layer. Likely several decades are needed for the dark slope streak to become completely brighter than the surrounding terrains. Model 2 illustrates a case where, with time, the fragile large grain agglomerates break down, perhaps due to external weathering or the wear-off of interparticle forces. In this schematic, the color of the grains is only symbolic and particle sizes are not to scale.

bright slope streaks in other regions than Arabia may be an indicator of variable dust thickness, dust deposition rates and/or cohesive soil properties on Mars.

Laboratory measurements of sieved Mars simulant samples of particle size fractions from <10 to 40 μm yielded reflectance ratios comparable to those observed by CaSSIS for dark and bright slope streaks. It suggests that particles found within and outside of slope streaks are perhaps different by several factors in size. Hapke reflectance modeling of palagonite dust indicated that the largest albedo increase occurs for the smallest particle size ranges (<10 μm grain size).

We have shown that slope streak surfaces are non-Lambertian (i.e. scatter light non uniformly with phase angle) and are susceptible to shadow hiding opposition effects. If low tau atmospheric conditions are available, optical phenomena can be observed on the Martian surface using CaSSIS. Since CaSSIS is able to image under extremely low phase angle illumination (<5°) perhaps coherent backscattering opposition effect can also be investigated for martian particulate materials. The observations of these optical phenomena will be analyzed within future work.

Author statement

A. Valantinas: Conceptualization, Resources, Methodology, Software, Visualization, Formal analysis, Writing - original draft, Investigation, Writing - review & editing. P. Becerra: Conceptualization, Methodology, Software, Investigation, Supervision, Writing - review & editing. A. Pommerol: Conceptualization, Methodology, Supervision, Writing - review & editing. L.L. Tornabene: Conceptualization, Writing - review & editing. L. Affolter: Investigation. G. Cremonese: Funding acquisition. E. Hauber: Methodology, Writing - review & editing. A.S. McEwen: Writing - review & editing. G. Munaretto: Writing - review & editing. M. Pajola: Writing - review & editing. A. Parkes Bowen: Writing - review & editing. M.R. Patel: Software, Writing - review & editing. V.G. Rangarajan: Writing - review & editing. N. Schorghofer: Writing - review & editing. N. Thomas: Resources, Supervision, Funding acquisition.

Declaration of competing interest

The authors declare that they have no known competing financial interests or personal relationships that could have appeared to influence the work reported in this paper.

Acknowledgements

The authors thank Mikhail Kreslavsky and one anonymous reviewer for constructive comments, and Angelo Pio Rossi for editorial handling. CaSSIS is a project of the University of Bern and funded through the Swiss Space Office via ESA's PRODEX programme. The instrument hardware development was also supported by the Italian Space Agency (ASI) (ASI-INAF agreement no. 2020-17-HH.O), INAF/Astronomical Observatory of Padova, and the Space Research Center (CSK) in Warsaw. Support from SGF (Budapest), the University of Arizona (Lunar and Planetary Lab.) and NASA are also gratefully acknowledged. Operations support from the UK Space Agency under grant ST/R003025/1 is also acknowledged. LLT wishes to personally acknowledge funding and support from the Canadian Space Agency (CSA) through their Planetary and Astronomy Missions Co-Investigator programme (19PACOI07) and the Canadian NSERC Discovery Grant programme (RGPIN 2020–06418).

Appendix A. Supplementary data

Supplementary data to this article can be found online at https://doi.org/10.1016/j.pss.2021.105373.

References

Aharonson, O., Schorghofer, N., Gerstell, M.F., 2003. Slope streak formation and dust deposition rates on Mars. J. Geophys. Res.: Planets 108 (E12). https://doi.org/10.1029/2003JE002123.

Ahn, J., Jung, J., 2017. Effects of fine particles on thermal conductivity of mixed silica sands. Appl. Sci. 7 (7). https://doi.org/10.3390/app7070650.

Allen, C.C., Jager, K.M., Morris, R.V., Lindstrom, D.J., Lindstrom, M.M., Lockwood, J.P., 1998. JSC mars-1: a martian soil simulant. Space 98, 469–476. https://doi.org/10.1061/40339(206)54.

Amador, E.S., Mushkin, A., Gillespie, A., 2016. Spectral characteristics of dark slope streaks on Mars: a global survey with CRISM (abstract # 2696). In: 47th Lunar and Planetary Science Conference.

Bagnold, R.A., 1954. Experiments on a gravity-free dispersion of large solid spheres in a Newtonian fluid under shear. Proc. Roy. Soc. Lond. Math. Phys. Sci. 225 (1160), 49–63. https://doi.org/10.1098/rspa.1954.0186.

Balme, M.R., Whelley, P.L., Greeley, R., 2003. Mars: dust devil track survey in Argyre Planitia and Hellas basin. J. Geophys. Res. Planets 108 (E8). https://doi.org/10.1029/2003JE002096.

Baratoux, D., Mangold, N., Forget, F., Cord, A., Pinet, P., Daydou, Y., Jehl, A., Masson, P., Neukum, G., The HRSC CO-Investigator Team, 2006. The role of the wind-transported dust in slope streaks activity: evidence from the HRSC data. Icarus 183 (1), 30–45. https://doi.org/10.1016/j.icarus.2006.01.023.

Becerra, P., Byrne, S., Brown, A.J., 2015. Transient bright "halos" on the south polar residual cap of mars: implications for mass-balance. Icarus 251, 211–225. https://doi.org/10.1016/j.icarus.2014.04.050.

Bergonio, J.R., Rottas, K.M., Schorghofer, N., 2013. Properties of martian slope streak populations. Icarus 225 (1), 194–199. https://doi.org/10.1016/j.icarus.2013.03.023.

Beyer, R.A., Chuang, F.C., Thomson, B.J., Milazzo, M.P., Wray, J., 2008. Martian slope streak brightening mechanisms (abstract # 2538). In: 39th Lunar and Planetary Science Conference.

Bhardwaj, A., Sam, L., Martín-Torres, F.J., Zorzano, M.-P., Fonseca, R.M., 2017. Martian slope streaks as plausible indicators of transient water activity. Sci. Rep. 7 (1). https://doi.org/10.1038/s41598-017-07453-9.

Blake, D.F., Morris, R.V., Kocurek, G., Morrison, S.M., Downs, R.T., Bish, D., Ming, D.W., Edgett, K.S., Rubin, D., Goetz, W., Madsen, M.B., Sullivan, R., Gellert, R., Campbell, I., Treiman, A.H., McLennan, S.M., Yen, A.S., Grotzinger, J., Vaniman, D.T., Chipera, S.J., Achilles, C.N., Rampe, E.B., Sumner, D., Meslin, P.-Y., Maurice, S., Forni, O., Gasnault, O., Fisk, M., Schmidt, M., Mahaffy, P., Leshin, L.A., Glavin, D., Steele, A., Freissinet, C., Navarro-González, R., Yingst, R.A., Kah, L.C., Bridges, N., Lewis, K.W., Bristow, T.F., Farmer, J.D., Crisp, J.A., Stolper, E.M., Des Marais, D.J., Sarrazin, P., et al., 2013. Curiosity at Gale crater, mars: characterization and analysis of the rocknest sand shadow. Science 341 (6153). https://doi.org/10.1126/science.1239505.

Bridges, N., Banks, M., Beyer, R., Chuang, F., Noe Dobrea, E., Herkenhoff, K., Keszthelyi, L., Fishbaugh, K., McEwen, A., Michaels, T., Thomson, B., Wray, J., 2010. Aeolian bedforms, yardangs, and indurated surfaces in the Tharsis Montes as seen by the HiRISE Camera: evidence for dust aggregates. Icarus 205 (1), 165–182. https://doi.org/10.1016/j.icarus.2009.05.017.

Brusnikin, E.S., Kreslavsky, M.A., Zubarev, A.E., Patratiy, V.D., Krasilnikov, S.S., Head, J.W., Karachevtseva, I.P., 2016. Topographic measurements of slope streaks on Mars. Icarus 278, 52–61. https://doi.org/10.1016/j.icarus.2016.06.005.

Cannon, K.M., Britt, D.T., Smith, T.M., Fritsche, R.F., Batcheldor, D., 2019. Mars global simulant MGS-1: a Rocknest-based open standard for basaltic martian regolith simulants. Icarus 317, 470–478. https://doi.org/10.1016/j.icarus.2018.08.019.

Chuang, F.C., Beyer, R.A., Bridges, N.T., 2010. Modification of martian slope streaks by eolian processes. Icarus 205 (1), 154–164. https://doi.org/10.1016/j.icarus.2009.07.035.

Chuang, F.C., Beyer, R.A., McEwen, A.S., Thomson, B.J., 2007. Hirise observations of slope streaks on Mars. Geophys. Res. Lett. 34 (20). https://doi.org/10.1029/2007GL031111.

Daubar, I., Dundas, C., Byrne, S., Geissler, P., Bart, G., McEwen, A., Russell, P., Chojnacki, M., Golombek, M., 2016. Changes in blast zone albedo patterns around new martian impact craters. Icarus 267, 86–105. https://doi.org/10.1016/j.icarus.2015.11.032.

Dickson, J.L., Kerber, L.A., Fassett, C.I., Ehlmann, B.L., 2018. A global, blended CTX mosaic of mars with vectorized seam mapping: a new mosaicking pipeline using principles of non-destructive image editing (Abstract # 2480). In: 49th Lunar and Planetary Science Conference.

Dundas, C.M., 2020a. An aeolian grainflow model for martian recurring slope lineae. Icarus 343, 113681. https://doi.org/10.1016/j.icarus.2020.113681.

Dundas, C.M., 2020b. Geomorphological evidence for a dry dust avalanche origin of slope streaks on Mars. Nat. Geosci. 13 (7), 473–476. https://doi.org/10.1038/s41561-020-0598-x.

Dundas, C.M., Becerra, P., Byrne, S., Chojnacki, M., Daubar, I.J., Diniega, S., Hansen, C.J., Herkenhoff, K.E., Landis, M.E., McEwen, A.S., Portyankina, G., Valantinas, A., 2021. Active mars: a dynamic world. J. Geophys. Res. Planets 126 (8). https://doi.org/10.1029/2021JE006876 e2021JE006876.

Ferguson, H.M., Lucchitta, B.K., 1984. Dark Streaks on Talus Slopes, Mars, pp. 188–190. NASA Tech. Memo., NASA TM-86246.

Fernando, J., Schmidt, F., Douté, S., 2016. Martian surface microtexture from orbital CRISM multi-angular observations: a new perspective for the characterization of the geological processes. Planet. Space Sci. 128, 30–51. https://doi.org/10.1016/j.pss.2016.05.005.

Geissler, P.E., 1992. Spectrophotometric Mapping of Coprates Quadrangle, Mars. The University of Arizona. PhD Thesis.

Gerstell, M.F., Aharonson, O., Schorghofer, N., 2004. A distinct class of avalanche scars on mars. Icarus 168 (1), 122–130. https://doi.org/10.1016/j.icarus.2003.11.005.

Greeley, R., Waller, D.A., Cabrol, N.A., Landis, G.A., Lemmon, M.T., Neakrase, L.D.V., Pendleton Hoffer, M., Thompson, S.D., Whelley, P.L., 2010. Gusev Crater, Mars: observations of three dust devil seasons. J. Geophys. Res.: Planets 115 (E7). https://doi.org/10.1029/2010JE003608.

Hapke, B., 1984. Bidirectional reflectance spectroscopy 3. Correction for macroscopic roughness. Icarus 59 (1), 41–59. https://doi.org/10.1016/0019-1035(84)90054-X.

Hapke, B., 2012. Theory of Reflectance and Emittance Spectroscopy, second ed. Cambridge University Press.

Harrison, R.G., Barth, E., Esposito, F., Merrison, J., Montmessin, F., Aplin, K.L., Borlina, C., Berthelier, J.J., Déprez, G., Farrell, W.M., Houghton, I.M.P., Renno, N.O., Nicoll, K.A., Tripathi, S.N., Zimmerman, M., 2016. Applications of electrified dust and dust devil electrodynamics to martian atmospheric electricity. Space Sci. Rev. 203, 299–345. https://doi.org/10.1007/s11214-016-0241-8.

Helfenstein, P., Veverka, J., Hillier, J., 1997. The lunar opposition effect: a test of alternative models. Icarus 128 (1), 2–14. https://doi.org/10.1006/icar.1997.5726.

Herkenhoff, K.E., Squyres, S.W., Anderson, R., Archinal, B.A., Arvidson, R.E., Barrett, J.M., Becker, K.J., Bell III, J.F., Budney, C., Cabrol, N.A., Chapman, M.G., Cook, D., Ehlmann, B.L., Farmer, J., Franklin, B., Gaddis, L.R., Galuszka, D.M., Garcia, P.A., Hare, T.M., Howington-Kraus, E., Johnson, J.R., Johnson, S., Kinch, K., Kirk, R.L., Lee, E.M., Leff, C., Lemmon, M., Madsen, M.B., Maki, J.N., Mullins, K.F., Redding, B.L., Richter, L., Rosiek, M.R., Sims, M.H., Soderblom, L.A., Spanovich, N., Springer, R., Sucharski, R.M., Sucharski, T., Sullivan, R., Torson, J.M., Yen, A., 2006. Overview of the microscopic imager investigation during spirit's first 450 sols in gusev crater. J. Geophys. Res. Planets 111 (E2). https://doi.org/10.1029/2005JE002574.

Herkenhoff, K.E., Squyres, S.W., Arvidson, R., Bass, D.S., Bell, J.F., Bertelsen, P., Cabrol, N.A., Gaddis, L., Hayes, A.G., Hviid, S.F., Johnson, J.R., Kinch, K.M., Madsen, M.B., Maki, J.N., McLennan, S.M., McSween, H.Y., Rice, J.W., Sims, M., Smith, P.H., Soderblom, L.A., Spanovich, N., Sullivan, R., Wang, A., 2004. Textures of the soils and rocks at gusev crater from spirit's microscopic imager. Science 305 (5685), 824–826. https://doi.org/10.1126/science.3050824.

Heyer, T., Kreslavsky, M., Hiesinger, H., Reiss, D., Bernhardt, H., Jaumann, R., 2019. Seasonal formation rates of martian slope streaks. Icarus 323, 76–86. https://doi.org/10.1016/j.icarus.2019.01.010.

Holmes, J.A., Lewis, S.R., Patel, M.R., 2020. OpenMars: a global record of martian weather from 1999 to 2015. Planet. Space Sci. 188, 104962. https://doi.org/10.1016/j.pss.2020.104962.

Johnson, J.R., Bell, J.F., Geissler, P., Grundy, W.M., Guinness, E.A., Pinet, P.C., Soderblom, J., 2008. Physical properties of the Martian surface from spectrophotometric observations. In: Bell, J. (Ed.), *The Martian Surface: Composition, Mineralogy and Physical Properties*, Cambridge Planetary Science. Cambridge University Press, pp. 428–450. https://doi.org/10.1017/CBO9780511536076.020.

Kleinhans, M., 2004. Sorting in grain flows at the lee side of dunes. Earth Sci. Rev. 65 (1), 75–102. https://doi.org/10.1016/S0012-8252(03)00081-3.

Kreslavsky, M.A., Head, J.W., 2009. Slope streaks on Mars: a new "wet" mechanism. Icarus 201 (2), 517–527. https://doi.org/10.1016/j.icarus.2009.01.026.

Malin, M.C., Bell III, J.F., Cantor, B.A., Caplinger, M.A., Calvin, W.M., Clancy, R.T., Edgett, K.S., Edwards, L., Haberle, R.M., James, P.B., Lee, S.W., Ravine, M.A., Thomas, P.C., Wolff, M.J., 2007. Context camera investigation on board the mars reconnaissance orbiter. J. Geophys. Res.: Planets 112 (E5). https://doi.org/10.1029/2006JE002808.

Malin, M.C., Edgett, K.S., 2001. Mars global surveyor mars orbiter camera: interplanetary cruise through primary mission. J. Geophys. Res.: Planets 106 (E10), 23429–23570. https://doi.org/10.1029/2000JE001455.

McCleese, D.J., Schofield, J.T., Taylor, F.W., Calcutt, S.B., Foote, M.C., Kass, D.M., Leovy, C.B., Paige, D.A., Read, P.L., Zurek, R.W., 2007. Mars climate sounder: an investigation of thermal and water vapor structure, dust and condensate distributions in the atmosphere, and energy balance of the polar regions. J. Geophys. Res.: Planets 112 (E5). https://doi.org/10.1029/2006JE002790.

McEwen, A.S., Dundas, C.M., Mattson, S.S., Toigo, A.D., Ojha, L., Wray, J.J., Chojnacki, M., Byrne, S., Murchie, S.L., Thomas, N., 2014. Recurring slope lineae in equatorial regions of Mars. Nat. Geosci. 7 (1), 53–58. https://doi.org/10.1038/ngeo2014.

McEwen, A.S., Eliason, E.M., Bergstrom, J.W., Bridges, N.T., Hansen, C.J., Delamere, W.A., Grant, J.A., Gulick, V.C., Herkenhoff, K.E., Keszthelyi, L., Kirk, R.L., Mellon, M.T., Squyres, S.W., Thomas, N., Weitz, C.M., 2007. Mars reconnaissance orbiter's high resolution imaging science experiment (hirise). J. Geophys. Res.: Planets 112 (E5). https://doi.org/10.1029/2005JE002605.

McEwen, A.S., Ojha, L., Dundas, C.M., Mattson, S.S., Byrne, S., Wray, J.J., Cull, S.C., Murchie, S.L., Thomas, N., Gulick, V.C., 2011. Seasonal flows on warm martian slopes. Science 333, 740–743. https://doi.org/10.1126/science.1204816.

Miyamoto, H., Dohm, J.M., Beyer, R.A., Baker, V.R., 2004. Fluid dynamical implications of anastomosing slope streaks on Mars. J. Geophys. Res.: Planets 109 (E6). https://doi.org/10.1029/2003JE002234.

Morris, E.C., 1982. Aureole deposits of the martian volcano Olympus Mons. J. Geophys. Res. Solid Earth 87 (B2), 1164–1178. https://doi.org/10.1029/JB087iB02p01164.

Muinonen, K., 1994. Coherent backscattering by solar system dust particles. In: Symposium - International Astronomical Union, 160, pp. 271–296. https://doi.org/10.1017/S0074180900046593.

Muinonen, K., Tyynelä, J., Zubko, E., Videen, G., 2010. Coherent backscattering in planetary regoliths. In: Kokhanovsky, A.A. (Ed.), Light Scattering Reviews 5: Single Light Scattering and Radiative Transfer. Springer Berlin Heidelberg, Berlin, Heidelberg, pp. 477–518. https://doi.org/10.1007/978-3-642-10336-0_11.

Munaretto, G., Pajola, M., Cremonese, G., Re, C., Lucchetti, A., Simioni, E., Mcewen, A., Pommerol, A., Becerra, P., Conway, S., Thomas, N., Massironi, D.M., 2020. Implications for the origin and evolution of martian recurring slope lineae at Hale crater from CaSSIS observations. Planet. Space Sci. 187, 104947. https://doi.org/10.1016/j.pss.2020.104947.

Munaretto, G., Pajola, M., Lucchetti, A., Re, C., Cremonese, G., Simioni, E., Cambianica, P., Thomas, N., 2021. Topographic correction of HiRISE and CaSSIS images: validation and application to color observations of Martian albedo features. Planet. Space Sci. 200, 105198. https://doi.org/10.1016/j.pss.2021.105198.

Murchie, S., Arvidson, R., Bedini, P., Beisser, K., Bibring, J.-P., Bishop, J., Boldt, J., Cavender, P., Choo, T., Clancy, R.T., Darlington, E.H., Des Marais, D., Espiritu, R., Fort, D., Green, R., Guinness, E., Hayes, J., Hash, C., Heffernan, K., Hemmler, J., Heyler, G., Humm, D., Hutcheson, J., Izenberg, N., Lee, R., Lees, J., Lohr, D., Malaret, E., Martin, T., McGovern, J.A., McGuire, P., Morris, R., Mustard, J., Pelkey, S., Rhodes, E., Robinson, M., Roush, T., Schaefer, E., Seagrave, G., Seelos, F., Silverglate, P., Slavney, S., Smith, M., Shyong, W.-J., Strohbehn, K., Taylor, H., Thompson, P., Tossman, B., Wirzburger, M., Wolff, M., 2007. Compact reconnaissance imaging spectrometer for mars (CRISM) on mars reconnaissance orbiter (MRO). J. Geophys. Res. Planets 112 (E5). https://doi.org/10.1029/2006JE002682.

Mushkin, A., Gillespie, A.R., Montgomery, D.R., Schreiber, B.C., Arvidson, R.E., 2010. Spectral constraints on the composition of low-albedo slope streaks in the Olympus Mons Aureole. Geophys. Res. Lett. 37 (22). https://doi.org/10.1029/2010GL044535.

Ody, A., Poulet, F., Langevin, Y., Bibring, J.-P., Bellucci, G., Altieri, F., Gondet, B., Vincendon, M., Carter, J., Manaud, N., 2012. Global maps of anhydrous minerals at the surface of Mars from OMEGA/MEx. J. Geophys. Res. Planets 117 (E11). https://doi.org/10.1029/2012JE004117.

Perry, J.E., Heyd, R., Read, M., Tornabene, L.L., Sutton, S., Byrne, S., Thomas, N., Fennema, A., McEwen, A., Berry, K., 2021. Geometric processing of TGO CaSSIS observations. Planet. Space Sci. Submitted for publication.

Phillips, C.B., Burr, D.M., Beyer, R.A., 2007. Mass movement within a slope streak on Mars. Geophys. Res. Lett. 34 (21). https://doi.org/10.1029/2007GL031577.

Pommerol, A., Jost, B., Poch, O., El-Maarry, M., Vuitel, B., Thomas, N., 2015. The SCITEAS experiment: optical characterizations of sublimating icy planetary analogues. Planet. Space Sci. 109–110, 106–122. https://doi.org/10.1016/j.pss.2015.02.004.

Pommerol, A., Thomas, N., Affolter, M., Portyankina, G., Jost, B., Seiferlin, K., Aye, K.-M., 2011. Photometry and bulk physical properties of solar system surfaces icy analogs: the planetary ice laboratory at University of bern. Planet. Space Sci. 59 (13), 1601–1612. https://doi.org/10.1016/j.pss.2011.07.009.

Ramsdale, J.D., Balme, M.R., Conway, S.J., Gallagher, C., van Gasselt, S.A., Hauber, E., Orgel, C., Séjourné, A., Skinner, J.A., Costard, F., Johnsson, A., Losiak, A., Reiss, D., Swirad, Z.M., Kereszturi, A., Smith, I.B., Platz, T., 2017. Grid-based mapping: a method for rapidly determining the spatial distributions of small features over very large areas. Planet. Space Sci. 140, 49–61. https://doi.org/10.1016/j.pss.2017.04.002.

Roloff, V., Pommerol, A., Gambicorti, L., et al., 2017. On-ground performance and calibration of the ExoMars Trace gas orbiter CaSSIS imager. Space Sci. Rev. 212, 1871–1896. https://doi.org/10.1007/s11214-017-0404-2.

Roush, T.L., 1994. Charon: more than water ice? Icarus 108 (2), 243–254. https://doi.org/10.1006/icar.1994.1059.

Ruff, S.W., Christensen, P.R., 2002. Bright and dark regions on Mars: particle size and mineralogical characteristics based on Thermal Emission Spectrometer data. J. Geophys. Res. Planets 107 (E12). https://doi.org/10.1029/2001JE001580.

Schaefer, E., McEwen, A., Sutton, S., 2019. A case study of recurring slope lineae (RSL) at Tivat crater: implications for RSL origins. Icarus 317, 621–648. https://doi.org/10.1016/j.icarus.2018.07.014.

Schorghofer, N., Aharonson, O., Gerstell, M., Tatsumi, L., 2007. Three decades of slope streak activity on Mars. Icarus 191 (1), 132–140. https://doi.org/10.1016/j.icarus.2007.04.026.

Schorghofer, N., King, C.M., 2011. Sporadic formation of slope streaks on Mars. Icarus 216 (1), 159–168. https://doi.org/10.1016/j.icarus.2011.08.028.

Shepard, M.K., Helfenstein, P., 2007. A test of the Hapke photometric model. J. Geophys. Res.: Planets 112 (E3). https://doi.org/10.1029/2005JE002625.

Shkuratov, Y.G., Helfenstein, P., 2001. The opposition effect and the Quasi-fractal structure of regolith: I. Theory. Icarus 152 (1), 96–116. https://doi.org/10.1006/icar.2001.6630.

Shkuratov, Y.G., Starukhina, L.V., Kreslavsky, M.A., Opanasenko, N.V., Stankevich, D.G., Shevchenko, V.G., 1994. Principle of undulatory invariance in photometry of atmosphereless celestial bodies. Icarus 109 (1), 168–190. https://doi.org/10.1006/icar.1994.1084.

Stillman, D.E., Michaels, T.I., Grimm, R.E., 2017. Characteristics of the numerous and widespread recurring slope lineae (rsl) in valles marineris, mars. Icarus 285, 195–210. https://doi.org/10.1016/j.icarus.2016.10.025.

Sullivan, R., Arvidson, R., Bell III, J.F., Gellert, R., Golombek, M., Greeley, R., Herkenhoff, K., Johnson, J., Thompson, S., Whelley, P., Wray, J., 2008. Wind-driven particle mobility on mars: insights from mars exploration rover observations at "El Dorado" and surroundings at gusev crater. J. Geophys. Res.: Planets 113 (E6). https://doi.org/10.1029/2008JE003101.

Sullivan, R., Thomas, P., Veverka, J., Malin, M., Edgett, K.S., 2001. Mass movement slope streaks imaged by the Mars Orbiter Camera. J. Geophys. Res.: Planets 106 (E10), 23607–23633. https://doi.org/10.1029/2000je001296.

Szwast, M.A., Richardson, M.I., Vasavada, A.R., 2006. Surface dust redistribution on mars as observed by the mars global surveyor and viking orbiters. J. Geophys. Res. Planets 111 (E11). https://doi.org/10.1029/2005JE002485.

Thomas, N., Cremonese, G., Ziethe, R., et al., 2017. The Colour and stereo surface imaging system (CaSSIS) for the ExoMars Trace gas orbiter. Space Sci. Rev. 212, 1897–1944. https://doi.org/10.1007/s11214-017-0421-1.

Thomas, P.C., Gierasch, P., Sullivan, R., Miller, D.S., Alvarez del Castillo, E., Cantor, B., Mellon, M.T., 2003. Mesoscale linear streaks on Mars: environments of dust entrainment. Icarus 162 (2), 242–258. https://doi.org/10.1016/S0019-1035(03)00028-9.

Vaughan, A.F., Johnson, J.R., Herkenhoff, K.E., Sullivan, R., Landis, G.A., Goetz, W., Madsen, M.B., 2010. Pancam and Microscopic Imager observations of dust on the Spirit Rover: cleaning events, spectral properties, and aggregates. MARS J 5, 129–145. https://doi.org/10.1555/mars.2010.0005.

Vincendon, M., 2013. Mars surface phase function constrained by orbital observations. Planet. Space Sci. 76, 87–95. https://doi.org/10.1016/j.pss.2012.12.005.

Vincendon, M., Pilorget, C., Carter, J., Stcherbinine, A., 2019. Observational evidence for a dry dust-wind origin of Mars seasonal dark flows. Icarus 325, 115–127. https://doi.org/10.1016/j.icarus.2019.02.024.

Viviano-Beck, C.E., Seelos, F.P., Murchie, S.L., Kahn, E.G., Seelos, K.D., Taylor, H.W., Taylor, K., Ehlmann, B.L., Wiseman, S.M., Mustard, J.F., Morgan, M.F., 2014. Revised CRISM spectral parameters and summary products based on the currently detected mineral diversity on Mars. J. Geophys. Res. Planets 119 (6), 1403–1431. https://doi.org/10.1002/2014JE004627.

Warell, J., Davidsson, B., 2010. A Hapke model implementation for compositional analysis of VNIR spectra of Mercury. Icarus 209 (1), 164–178. https://doi.org/10.1016/j.icarus.2009.11.037.

Wells, E., Veverka, J., Thomas, P., 1984. Mars: experimental study of albedo changes caused by dust fallout. Icarus 58 (3), 331–338. https://doi.org/10.1016/0019-1035(84)90079-4.

Williams, S.H., 1991. Dark talus streaks on mars are similar to aeolian dark streaks (abstract # 1509). In: 22nd Lunar and Planetary Science Conference.

Wolff, M.J., Smith, M.D., Clancy, R.T., Arvidson, R., Kahre, M., Seelos IV, F., Murchie, S., Savijärvi, H., 2009. Wavelength dependence of dust aerosol single scattering albedo as observed by the Compact Reconnaissance Imaging Spectrometer. J. Geophys. Res.: Planets 114 (E2). https://doi.org/10.1029/2009JE003350.

Yoldi, Z., Pommerol, A., Poch, O., Thomas, N., 2021. Reflectance study of ice and Mars soil simulant associations – I. H2O ice. Icarus 358, 114169. https://doi.org/10.1016/j.icarus.2020.114169.